Design and performance estimates for the l'OASIS experiment magnetic spectrometers

G. Dugan,* A. Misuri,† and W. Leemans
Center for Beam Physics, Lawrence Berkeley National Laboratory, Berkeley, CA 94708‡
(Dated: November 19, 2001)

Two double-focusing magnetic spectrometers will be used to momentum analyze the electron beam produced by the l'OASIS laser plasma wakefield accelerator. One spectrometer, based on a round pole magnet, has an operating range up to 50 MeV/c, with a resolution in the 1-2% range. The other spectrometer, based on a wedge dipole magnet, has better resolution (about 0.5%) but an operating range limited to below 18 MeV/c. This note describes the optical design of the spectrometers, and provides detailed estimates of performance features such as dynamic range, operating range, calibration, resolution, acceptance, and aberrations

I. INTRODUCTION

In this note, the design of two double-focusing magnetic spectrometers is described, and the spectrometer performance is detailed. The spectrometers are to be used for the momentum analysis of electrons produced from the l'OASIS laser wakefield plasma accelerator. A schematic layout of the spectrometer system is shown in Fig. 1, which indicates all the spectrometer-related components and distances, but is not to scale. A to-scale drawing is shown in Fig. 2. The first spectrometer magnet, called the "round pole magnet", is a model 3473-70 GMW Associates Laboratory Electromagnet. The pole cap is cylindrical, with a 150 mm diameter. The second spectrometer magnet, called the "pacman magnet", is a standard wedge-pole C-dipole.

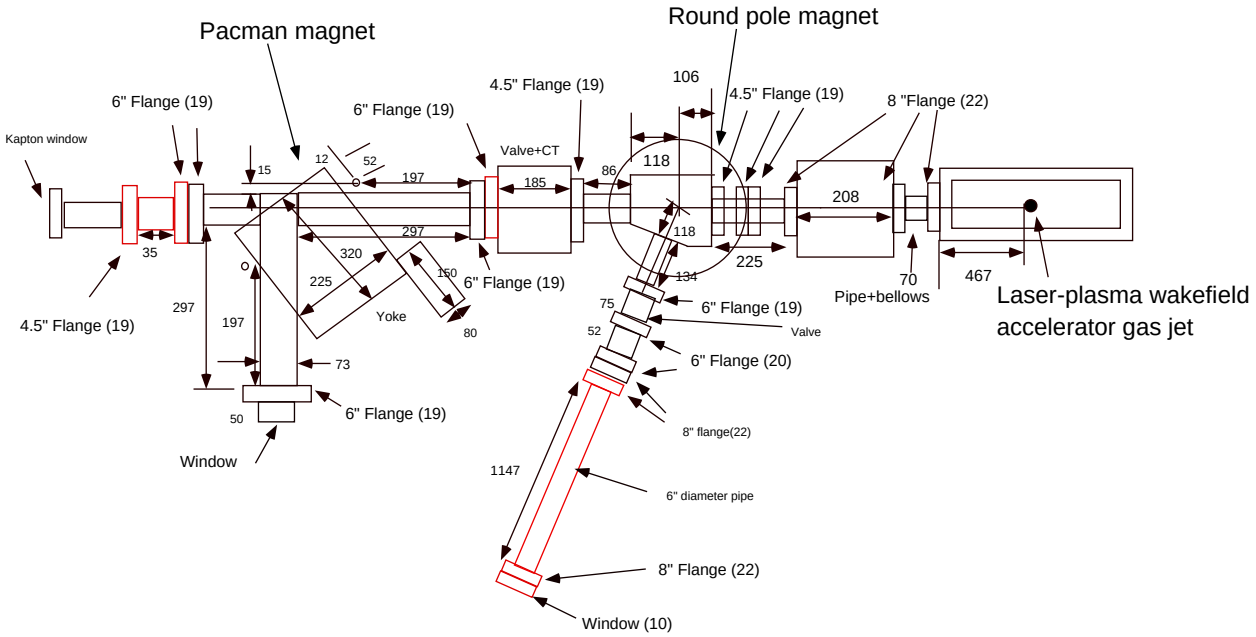

FIG. 1: Layout of the round pole and pacman spectrometers (not to scale) All dimensions in mm

*also at Laboratory for Nuclear Studies, Cornell University, Ithaca, NY 14853
†also at C.N.R and University of Pisa, Italy
‡Supported by the Department of Energy

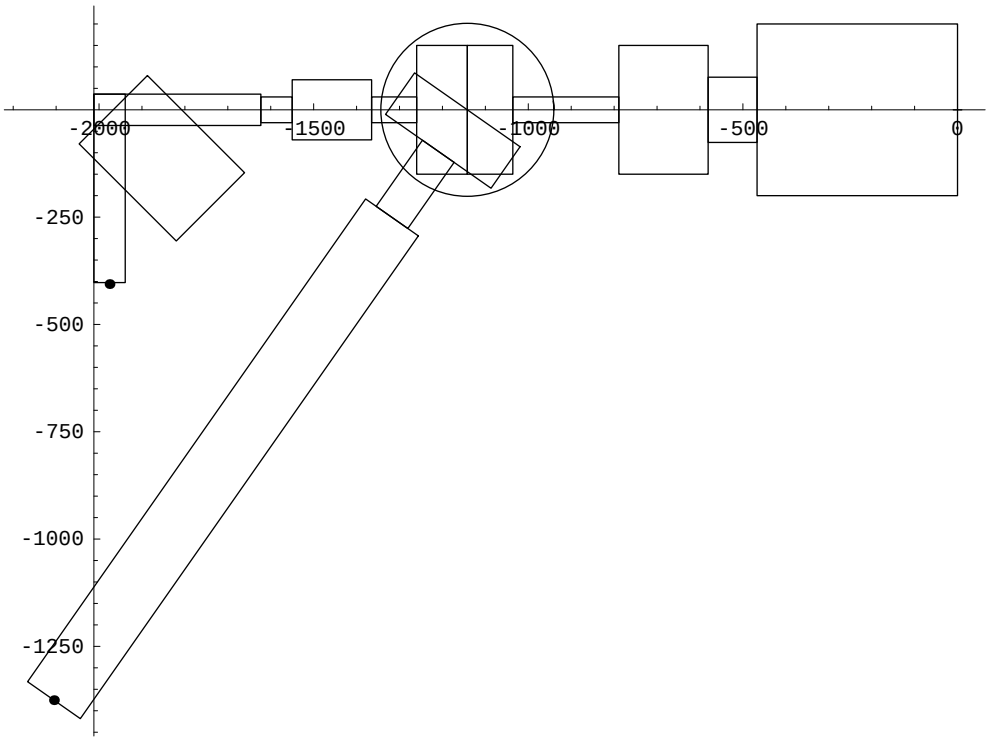

FIG. 2: Layout of the round pole and pacman spectrometers (to scale). The black dots indicate the calculated positions of the horizontal focus. Dimensions are in mm

II. TRANSPORT MATRICES FOR WEDGE BENDING MAGNETS

The standard formalism for the first-order optical properties of wedge bending magnets is given in [1, 2]. The general geometry is shown in Fig. 3, taken from [1]. The first-order thick lens transport through the body of a

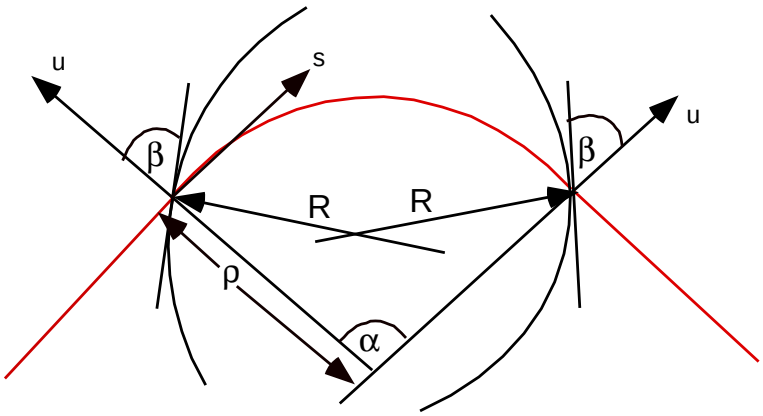

FIG. 3: Geometry of a symmetric wedge bending magnet

uniform field wedge magnet is given by

$$\mathbf{X}(s+\rho\alpha) = \mathbf{M}_{body}(\alpha,\rho)\,\mathbf{X}(s)$$

in which

$$\mathbf{X}(s) = \begin{pmatrix} x \\ x' \\ z \\ z' \\ \delta l \\ \frac{\delta p}{p} \end{pmatrix}, \quad \mathbf{M}_{body}(\alpha, \rho) = \begin{pmatrix} \cos\alpha & \rho\sin\alpha & 0 & 0 & 0 & \rho(1-\cos\alpha) \\ -\frac{\sin\alpha}{\rho} & \cos\alpha & 0 & 0 & 0 & \sin\alpha \\ 0 & 0 & 1 & \rho\alpha & 0 & 0 \\ 0 & 0 & 0 & 1 & 0 & 0 \\ \sin\alpha & \rho(1-\cos\alpha) & 0 & 0 & 1 & \rho(\alpha-\sin\alpha) \\ 0 & 0 & 0 & 0 & 0 & 1 \end{pmatrix}$$

In these equations, the z coordinate is out of the page, δl is the path length difference from the reference trajectory, and $\frac{\delta p}{p}$ is the relative momentum difference from the central momentum. In the thin lens (impulse) approximation, the first order edge focusing is described by the matrix

$$\mathbf{M}_{edge}(\beta, \rho) = \begin{pmatrix} 1 & 0 & 0 & 0 & 0 & 0 \\ \frac{\tan\beta}{\rho} & 1 & 0 & 0 & 0 & 0 \\ 0 & 0 & 1 & 0 & 0 & 0 \\ 0 & 0 & -\frac{\tan(\beta-\psi)}{\rho} & 1 & 0 & 0 \\ 0 & 0 & 0 & 0 & 1 & 0 \\ 0 & 0 & 0 & 0 & 0 & 1 \end{pmatrix}$$

The edge angle β is shown in Fig. 3. For positive β, the edges are defocusing in the bend plane and focusing in the non-bend plane. The angle ψ corrects for the finite length fringe field associated with a finite magnet gap G. To lowest order in $\frac{G}{\rho}$, it is given by

$$\psi = \frac{KG}{\rho}\left(1 + \sin^2\beta\right)$$

in which K is given by the following integral over the fringing field of the magnet,

$$K = \frac{1}{GB_0^2}\int_{end} ds B_z(s)\left[B_0 - B_z(s)\right], \tag{1}$$

where $B_0 = B_z(0)$ is the central field. $K = \frac{1}{6}$ for a linear fringe field. The overall transport through the magnet is described by

$$\mathbf{M}(\beta, \rho) = \mathbf{M}_{edge}(\beta, \rho)\,\mathbf{M}_{body}(\alpha, \rho)\,\mathbf{M}_{edge}(\beta, \rho)$$

III. DESIGN OF THE ROUND POLE SPECTROMETER

A. Geometry and linear optics

Fig. 4 illustrates the geometry of the round pole magnet, for which we assume that the magnetic field is azimuthally symmetric. (This assumption is supported by three-dimensional ANSYS magnetic field calculations, and also by comparisons between the field measurements, discussed below, and a two-dimensional POISSON model of the magnetic field)[3, 4].

The simplest model for the field corresponds to a hard-edge model in which a uniform vertical field of magnitude B_0 extends out from the origin of the Cartesian coordinate system to an effective radius R. For a given particle momentum p, the bending radius ρ is given in terms of the central field B_0 and the momentum by

$$B_0\rho\,[\mathrm{T\,m}] = \frac{p\left[\frac{\mathrm{GeV}}{\mathrm{c}}\right]}{0.2998} \tag{2}$$

For a given field (i.e, fixed B_0 and R), a given bend angle α, and a given value of the parameter Δ (see Fig. 4), there is a unique value of the bend radius corresponding to the trajectory illustrated in Fig. 4. The bend radius can be found from the geometry given in Fig. 4. We have

$$L = 2\rho\sin\frac{\alpha}{2},$$

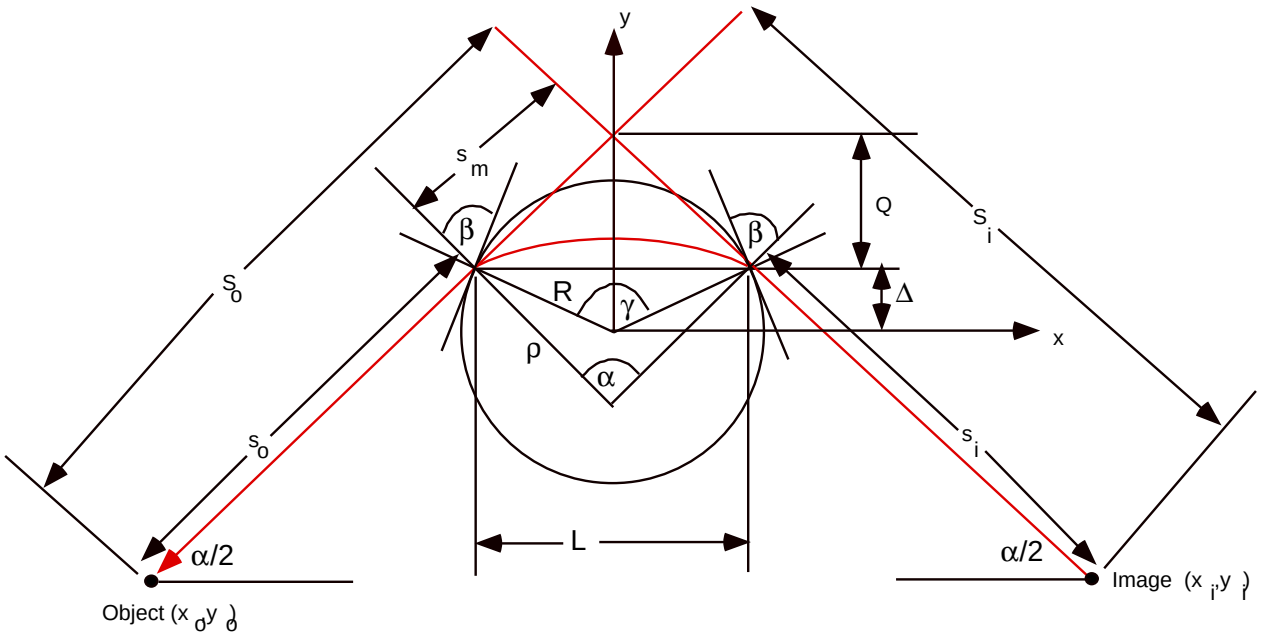

FIG. 4: Geometry of the round pole magnet. The ideal trajectory, and its extensions, is shown in red.

and

$$L^2 = 4\left(R^2 - \Delta^2\right).$$

So we have for the bend radius

$$\rho = \frac{\sqrt{R^2 - \Delta^2}}{\sin\frac{\alpha}{2}}$$

The central momentum for this bend radius can then be calculated from Eq. (2).

This value of the bend radius can then be substituted into the transport matrices described in Section II to compute the optics. From the geometry shown in Fig. 4, we have

$$2\rho\sin\frac{\alpha}{2} = 2R\sin\frac{\gamma}{2} \Rightarrow \gamma = 2\sin^{-1}\left(\frac{\rho}{R}\sin\frac{\alpha}{2}\right) = 2\sin^{-1}\left(\frac{\sqrt{R^2-\Delta^2}}{R}\right)$$

and

$$\beta = \frac{\pi + \alpha - \gamma}{2}$$

The parameter Δ, which determines where the trajectory transits the magnet, is the only free parameter. The "design" of this spectrometer then consists of finding a value of Δ corresponding to the condition of double focusing at the image point. This value will depend on the distance s_o. In practice, what is fixed is the distance between the object and the intersection of the incoming and outgoing trajectories, i.e., the distance $S_o = s_o + s_m$ in Fig. 4. This distance will be called the object distance. The distance s_o may be derived from this using

$$s_m = \rho\tan\frac{\alpha}{2} \Rightarrow \; s_o = S_o - \rho\tan\frac{\alpha}{2}$$

The coordinates of the object are given by

$$x_o = -s_o\cos\frac{\alpha}{2} - \rho\sin\frac{\alpha}{2} = -S_o\cos\frac{\alpha}{2} \tag{3}$$

$$y_o = -s_o\sin\frac{\alpha}{2} + \Delta = -S_o\sin\frac{\alpha}{2} + Q + \Delta \tag{4}$$

in which $Q = \rho \sin\frac{\alpha}{2} \tan\frac{\alpha}{2}$. The coordinates of the image are

$$x_i = s_i \cos\frac{\alpha}{2} + \rho \sin\frac{\alpha}{2} = S_i \cos\frac{\alpha}{2}$$
$$y_i = -s_i \sin\frac{\alpha}{2} + \Delta$$

in which $S_i = s_i + s_m$ is the image distance. The overall transport matrix from object to image is given by

$$\mathbf{T}(s_i, s_o) = \mathbf{D}(s_i)\,\mathbf{M}(\beta, \rho)\,\mathbf{D}(s_o) \tag{5}$$

in which

$$\mathbf{D}(s) = \begin{pmatrix} 1 & s & 0 & 0 & 0 & 0 \\ 0 & 1 & 0 & 0 & 0 & 0 \\ 0 & 0 & 1 & s & 0 & 0 \\ 0 & 0 & 0 & 1 & 0 & 0 \\ 0 & 0 & 0 & 0 & 1 & 0 \\ 0 & 0 & 0 & 0 & 0 & 1 \end{pmatrix}$$

is the matrix for a drift space. The requirements for point-to-point focus at the image point in the bend plane and non-bend plane are, respectively,

$$T_{12}(s_{iu}, s_o) = 0$$
$$T_{34}(s_{iz}, s_o) = 0 \tag{6}$$

These equations may be solved to give the distances s_{iu} and s_{iz} for a focus in the bend plane and non-bend plane. When $s_{iu} = s_{iz}$ we have the required double focus condition. The focal lengths of the magnet itself in the bend and non-bend plane are given respectively by

$$f_u = -\frac{1}{M_{21}} \qquad f_z = -\frac{1}{M_{43}}.$$

Measurements of the magnetic field of the round pole magnet were made using a Hall probe. These data may be used to find the value of the effective radius R. Fig. 5 shows the measured magnetic field B_z vs. r.

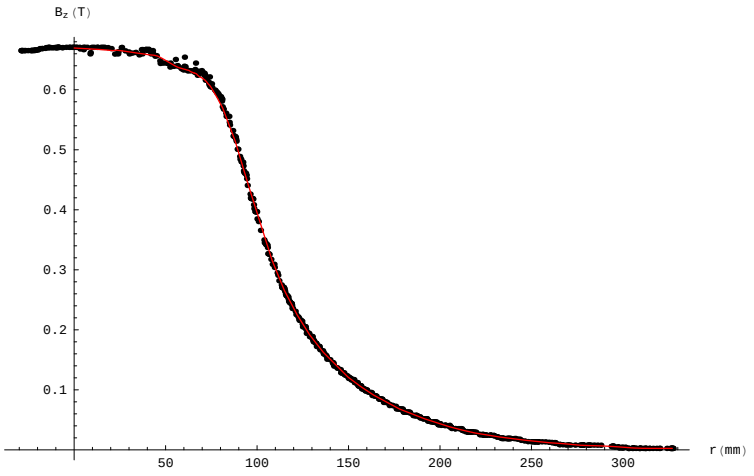

FIG. 5: Measured vertical magnetic field vs. radius for the round pole magnet, for a current of 35 A. The dots are the measured data, and the red line is an exponentially smoothed interpolation function used in the numerical calculation of the trajectories.

The effective radius is defined by

$$R = \frac{\int_0^\infty B_z(r)\,dr}{B_z(0)}$$

From the data shown in Fig. 5, we find R=117.3 mm. From Fig. 1, the object distance is S_o=1.142 m. The bend angle imposed by the vacuum chamber is $\alpha = 55°$. The central field (see Fig. 5) is B_0 =0.67 T (corresponding to 35 A in the magnet). The magnet gap is G=58 mm, and the value of K computed from Fig. 5 using Eq. (1) is K=0.4175.

Using these values, Fig. 6 gives the central momentum, Fig. 7 the focal lengths f_u and f_z, and Fig. 8 the image distances S_{iu} and S_{iz}, vs. the parameter Δ. For Δ=-20.23 mm, the image distances in both planes are equal, at $S_{iu} = S_{iz}$ =1.675 m. The central momentum at this value of Δ is 50.26 MeV/c.

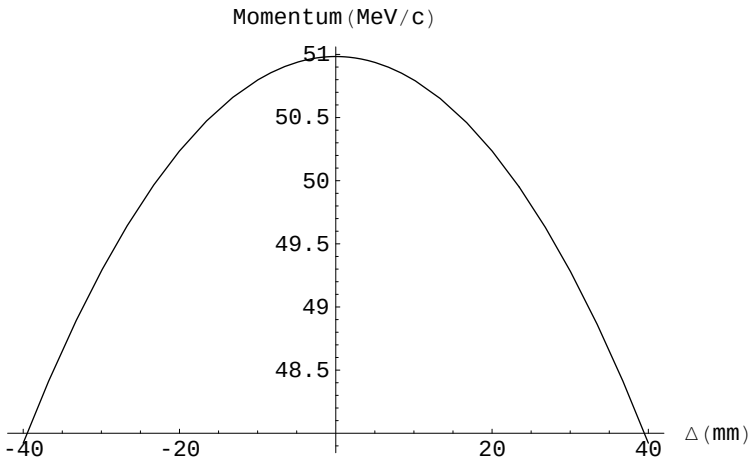

FIG. 6: Central momentum vs. Δ

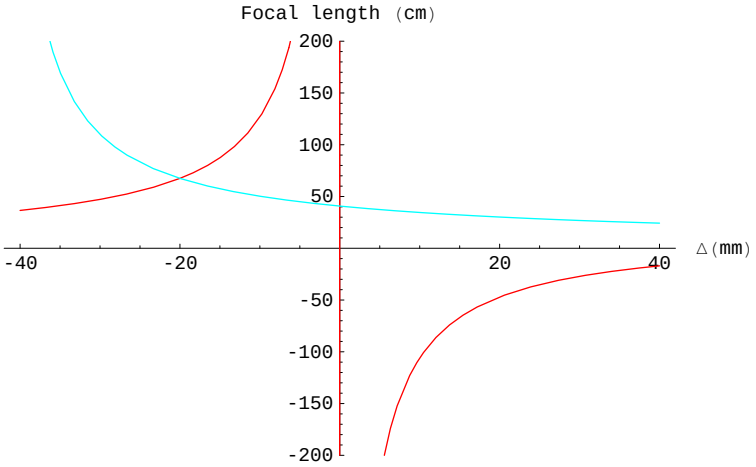

FIG. 7: Focal lengths vs. Δ. Blue corresponds to the non-bend plane, red to the bend plane.

B. Linear lattice functions

Considering the spectrometer system to be a beam transport line, the linear lattice functions β_x, β_y, and the momentum dispersion η may be calculated from the transport matrices. The initial value of the lattice functions β_0 (taken to be the same in both planes) may be estimated by making some assumptions about the initial beam phase space. The full angular spread of the beam from the laser plasma wakefield accelerator can be as large as 40 mrad. However, as discussed below, the spectrometer cannot transmit this large angular spread without very significant optical aberrations. So, we will assume that the beam is collimated to an rms angular spread of σ_0'=0.010 rad. We take the initial rms beam size to be roughly that of the laser spot σ_0 = 6 μm. Then $\beta_0 = \frac{\sigma_0}{\sigma_0'}$ = 0.6 mm. The corresponding geometric emittance is $\varepsilon = \sigma_0\sigma_0'$ = 0.06 μm. We also assume no initial position-angle correlation. Then we can calculate the evolution of the lattice functions, and the associated beam sizes, through the spectrometer. Fig. 9 shows the lattice functions, and Fig. 10 the beam

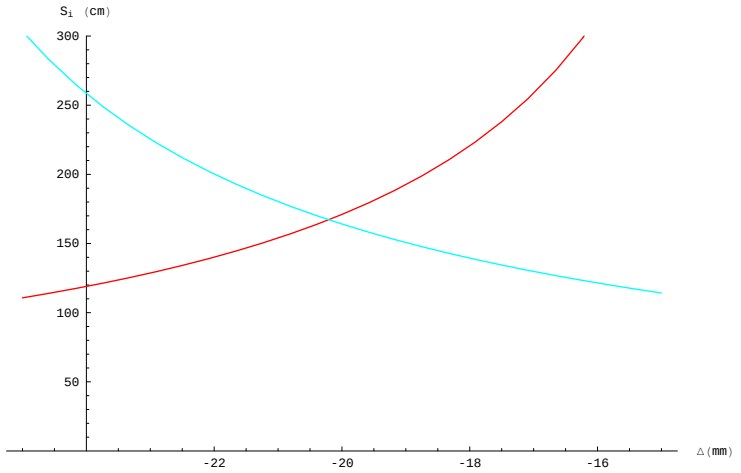

FIG. 8: Distances S_{iu} (red) and S_{iu} (blue) vs Δ. Blue corresponds to the non-bend plane, red to the bend plane.

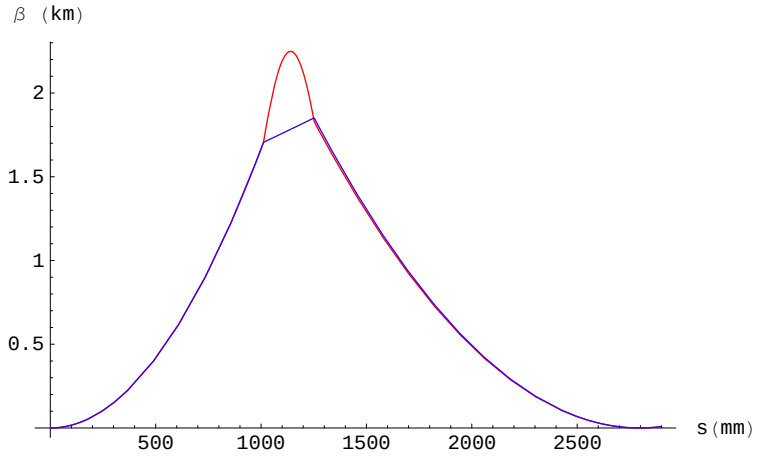

FIG. 9: Lattice functions β_x (red) and β_y (blue) for the round pole spectrometer system

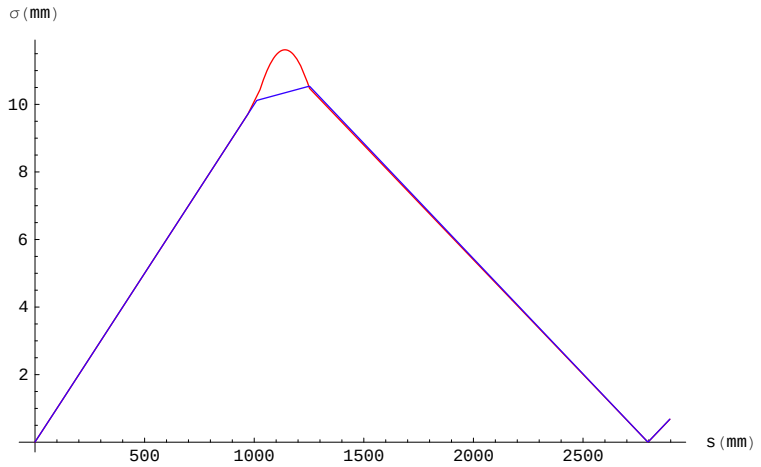

FIG. 10: Rms beam sizes σ_x (red) and σ_y (blue) for the round pole spectrometer system

sizes, given by $\sigma = \sqrt{\varepsilon\beta}$. Because of the very large aspect ratio of the initial phase space, the lattice function β rises to a more than a km before being brought down by the spectrometer magnet focusing field. The dispersion is shown in Fig. 11.

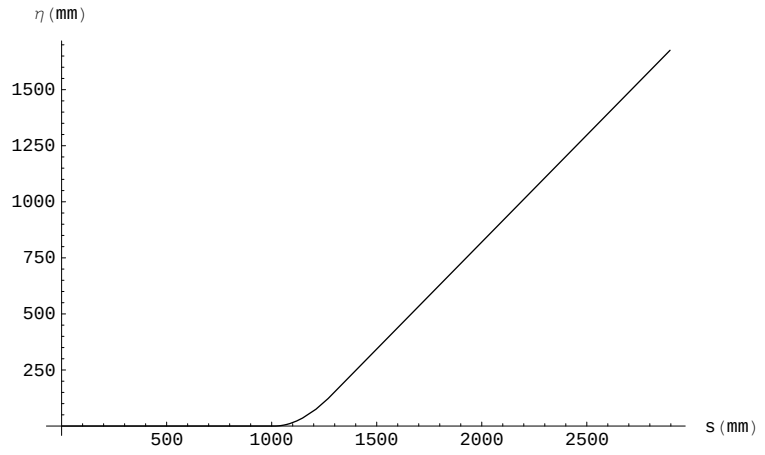

FIG. 11: Dispersion function η for the round pole spectrometer system

C. Direct integration of the equations of motion

1. Numerical solution technique

As Fig. 5 shows, the magnetic field of the round pole magnet is mostly fringe. Given this situation, it is unclear how well the thin lens approximation for the fringing field will work. Therefore, it seemed prudent to check the first order results by a direct solution of the equations of motion. This will also automatically include all geometric and chromatic aberrations. The equation of motion for an electron of charge $-e$, momentum $\mathbf{p}$, and velocity $\mathbf{v}$, in a field $\mathbf{B}$, is

$$\frac{d\mathbf{p}}{dt} = -e\mathbf{v} \times \mathbf{B}$$

In the Cartesian coordinate system shown in Fig. 4 (positive z is out of the paper), the equations of motion become

$$\begin{aligned} x'' &= -\frac{1}{(B_0\rho)}\left[y'B_z - z'B_y\right] \\ y'' &= -\frac{1}{(B_0\rho)}\left[z'B_x - x'B_z\right] \\ z'' &= -\frac{1}{(B_0\rho)}\left[x'B_y - y'B_x\right] \end{aligned}$$

in which primes denote differentiation along the trajectory coordinate $l = vt$. $B_0\rho$ is given by Eq. (2). The fields to be used in these equations may be derived from the field shown in Fig. 5, with the following assumptions. As noted above, we assume azimuthal symmetry in a cylindrical coordinate system centered on the origin shown in Fig. 4. We also assume midplane symmetry, so that the vertical component of the magnetic field may be written in the form

$$B_z\left(r,z\right) = B_{z0}\left(r\right) + B_{z1}\left(r\right)z^2 + ...$$

Keeping only the terms shown in the previous equation, and requiring that the field satisfies the Maxwell equations

$$\nabla \times \mathbf{B} = \nabla \cdot \mathbf{B} = 0$$

leads to the following result for the radial field component:

$$B_r\left(r,z\right) = z\frac{dB_{z0}}{dr} + \frac{z^3}{3}\frac{dB_{z1}}{dr} + ...$$

and the following expression for B_{z1}:

$$B_{z1}(r) = -\frac{1}{2}\left[\frac{1}{r}\frac{dB_{z0}}{dr} + \frac{d^2B_{z0}}{dr^2}\right].$$

The field components in the Cartesian system are given by

$$B_x(x,y,z) = \frac{xB_r\left(\sqrt{x^2+y^2}, z\right)}{\sqrt{x^2+y^2}}$$
$$B_y(x,y,z) = \frac{yB_r\left(\sqrt{x^2+y^2}, z\right)}{\sqrt{x^2+y^2}}$$
$$B_z(x,y,z) = B_z\left(\sqrt{x^2+y^2}, z\right)$$

Using these relations in the trajectory equations will treat the fringe field correctly to all orders in x and y, and to third order in z.

The equations of motion have been solved using Mathematica's **NDSolve** function, starting at the point given by Eqs. (3) and (4). The solution is obtained iteratively as follows. For given values of Δ and S_o, and a trial value of ρ, the trajectory is calculated, and the total bend angle is determined. The value of ρ is then adjusted to make the total bend angle equal to $\alpha = 55°$. This determines the reference trajectory and central momentum for the chosen value of Δ. To evaluate the focusing properties of the system, we must first transform from the (x, y) system to the curvilinear coordinate system in the bend plane (u, s) shown in Fig. 3. The orthogonal coordinate of a point (x, y) is

$$u(x,y,s) = (y - y_0(s))\cos\theta(s) - (x - x_0(s))\sin\theta(s)$$

in which $(x_0(s), y_0(s))$ is the reference trajectory, given numerically as described above, and $\tan\theta(s) = \frac{y'(s)}{x'(s)}$. The orthogonal coordinate of a general trajectory is $u(x(l), y(l), s)$ in the bend plane, and $z(l)$ in the non-bend plane. To evaluate these in terms of the reference trajectory coordinate s, we use

$$l = s + \delta l,$$

in which δl is the first order path length difference, given implicitly by Eq. (5). Explicitly, for $s > s_o + \rho\alpha$, we have

$$\delta l = x(0)\sin\alpha + x'(0)\left(\rho(1-\cos\alpha) + s_o\sin\alpha\right) + \frac{\delta p}{p}\rho(\alpha - \sin\alpha)$$

We will neglect higher order terms in the dependence of the path length on the initial coordinates.

A trajectory which initially deviates from the reference trajectory by a transverse displacement u_0 and a small transverse angle u_0' has initial x, y coordinates and angles

$$x(0) = x_o - u_0\sin\theta_0,\ \ y(0) = y_o + u_0\cos\theta_0$$
$$x'(0) = \cos\theta_0 - u_0'\sin\theta_0,\ \ y'(0) = \sin\theta_0 + u_0'\cos\theta_0.$$

The trajectory equations may be solved with these initial conditions. Let us call the resulting trajectory coordinate orthogonal to the reference trajectory at the image $u_i(u_0, u_0', s)$. For a point-to-point focus, the image point in the bend plane then occurs at a coordinate $S_{tot,u}$ given by the solution of the equation

$$u_i(0, u_0', S_{tot,u}) = u_i(0, -u_0', S_{tot,u}).$$

A similar relation gives the image coordinate in the non-bend plane:

$$z_i(0, z_0', S_{tot,z}) = z_i(0, -z_0', S_{tot,z})$$

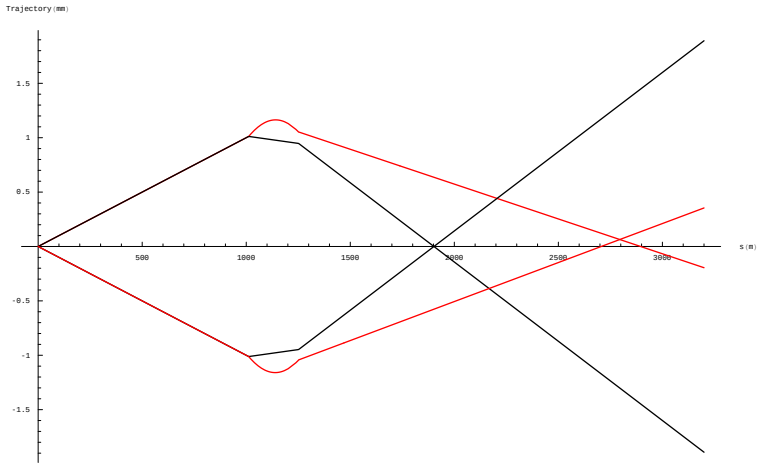

FIG. 12: Trajectories computed by numerical integration, for an idealized field, as a check on the numerical solution.The red curves correspond to trajectories in the bend plane, relative to the reference trajectory; the initial values are $u_0' = \pm 1$ mrad. The black curves are trajectories in the non-bend plane, corresponding to $z_0' = \pm 1$ mrad.

2. Test of the numerical technique

As a check of the numerical integration routines, the central trajectory has been computed for the following idealized field:

$$B_z\left(r,z\right) = \left\{ \begin{array}{c} B_0 \ \text{ if } r < R_0 \\ 0 \text{ if } r \geq R_0 \end{array} \right\}$$

$$B_r\left(r,z\right) = \left\{ \begin{array}{c} 0 \ \text{ if } r < R_0 - \frac{G}{2} \\ -\frac{zB_0}{G} \ \text{ if } R_0 - \frac{G}{2} \leq r < R_0 + \frac{G}{2} \\ 0 \ \text{ if } r \geq R_0 + \frac{G}{2} \end{array} \right\}$$

This field corresponds to the assumption made in deriving the first-order transport matrices: a uniform B_z field with a hard edge, and a B_r fringe field providing vertical focusing. The edge focusing matrix given above in Section II. assumes the thin lens approximation, so we must take the magnet gap to be small compared to the bend radius (about 250 mm). We take G=5 mm, and take $K = \frac{1}{6}$, appropriate for a linear fringe field. Otherwise, we use the geometry in Fig. 1 (S_o=1142 mm) and the field parameters used in Sec. III A (B_0=0.67 T, R=117.3 mm). We also take $\Delta = -20.23$ mm.

The central trajectory is numerically calculated and the bending radius associated with a 55° bend calculated as described above. The result gives a central momentum of 50.26 MeV/c, just as in the linear case.

Fig. 12 shows four trajectories, computed by numerical solution of the differential equations of motion. The red curves correspond to trajectories in the bend plane, relative to the reference trajectory; the initial values are $u_0' = \pm 1$ mrad. The black curves are trajectories in the non-bend plane, corresponding to $z_0' = \pm 1$ mrad. The bend plane images at $S_{tot,u} = 2.796$ m from the object. Note that the trajectories do not intersect at zero offset; this is due to horizontal aberrations. In the non-bend plane, the image is at $S_{tot,z} = 1.903$ m.

The distance S_{tot} is the total distances along the reference trajectory. To relate this to the image distance S_i, we use

$$S_{tot} = s_o + \rho\alpha + s_i = S_o + \rho\alpha + S_i - 2\rho\tan\frac{\alpha}{2} \Rightarrow$$

$$S_i = S_{tot} - \left(S_o + \rho\alpha - 2\rho\tan\frac{\alpha}{2}\right)$$

Using this equation, we find that the image distances S_i in the bend and non-bend plane, are, respectively, 1.674 m and 0.782 m. The linear optics equations predict respective values of 1.675 m and 0.785 m, in good agreement. The vertical focus is much close to the object here than in the solution described in Section III A because of the much shorter idealized fringe field, required to make a sensible comparison between the numerical solution and the thin-lens edge transport matrix.

3. Application to the measured field of the round pole magnet

The central trajectory was then numerically calculated using an exponentially smoothed interpolation function to represent the measured magnetic field (see Fig. 5), starting at S_o=1142 mm, and for $\alpha = 55°$. For several values of Δ, the bending radius associated with a 55° bend was calculated as described above, and the position of the focus in the bend plane and the non-bend plane was calculated. It was found that for Δ =-19.1 mm, both foci occurred at almost the same image distance. For this value of Δ, the central momentum was found to be 49.74 MeV/c.

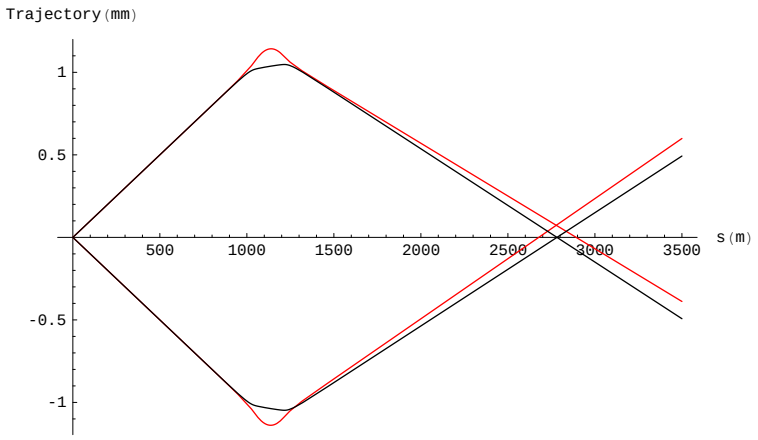

FIG. 13: Trajectories computed by numerical integration, for the measured field, for Δ=-19.1 mm. The red curves correspond to trajectories in the bend plane, relative to the reference trajectory; the initial values are $u_0' = \pm 1$ mrad. The black curves are trajectories in the non-bend plane, again corresponding to $z_0' = \pm 1$ mrad.

Fig. 13 shows four trajectories, computed by numerical solution for this value of Δ. The red curves correspond to trajectories in the bend plane, relative to the reference trajectory; the initial values are $u_0' = \pm 1$ mrad. The black curves are trajectories in the non-bend plane, corresponding to $z_0' = \pm 1$ mrad. The bend and non-bend plane image at $(S_{tot,u}, S_{tot,z}) = (2.785, 2.782)$ m from the object.

The distance S_{tot} is the total distance along the reference trajectory, which is no longer circular within the magnet. The image distance S_i must be computed in this case as follows:

$$S_i = \sqrt{\left(x_0\left(S_{tot}\right)\right)^2 + \left(y_0\left(S_{tot}\right) - \rho \sin\frac{\alpha}{2}\tan\frac{\alpha}{2} - \Delta\right)^2}$$

Using this equation, we find image distances of $(S_{iu}, S_{iz}) = (1.668, 1.664)$ m. From Fig. 1, the phosphor for viewing the beam is located at S=1661 mm, 5 mm from the average focal point. The geometry and first order optical properties of the round pole spectrometer are summarized in Tables I and II.

TABLE I: Round pole spectrometer geometrical parameters for the double focusing condition

Magnet	α deg.	β deg.	ρ mm	B_0 T	p_0 MeV/c	G mm	K	R mm	L mm	Δ mm
Hard edge approx.	55	17.57	250.228	0.67	50.26	58	0.4175	117.3	231.09	-20.23
Exact num. integ.	55	18.042	247.79	0.67	49.744			116.0	228.83	-19.06

4. Round pole magnet alignment

Fig. 14 shows the trajectories in the vicinity of the round pole magnet. In order for the central trajectory to enter the magnet at the required value of Δ for double focusing, the relative position of the vacuum chamber and the round pole magnet had to be adjusted slightly from its original position. In Fig. 14, the original center

TABLE II: Round pole spectrometer first order optical parameters for the double focusing condition

Magnet	S_0 mm	f_u mm	f_z mm	S_{iu} mm	S_{iz} mm	$T_{11}\,(s_{iu}, s_o)^a$	$T_{33}\,(s_{iz}, s_o)$ ^{b}
Hard edge approx.	1142	669.4	680.4	1674.5	1674.5	-1.47	-1.46
Exact num. integ.	1142			1668.4	1664.47		

[a]Horizontal magnification
[b]Vertical magnification

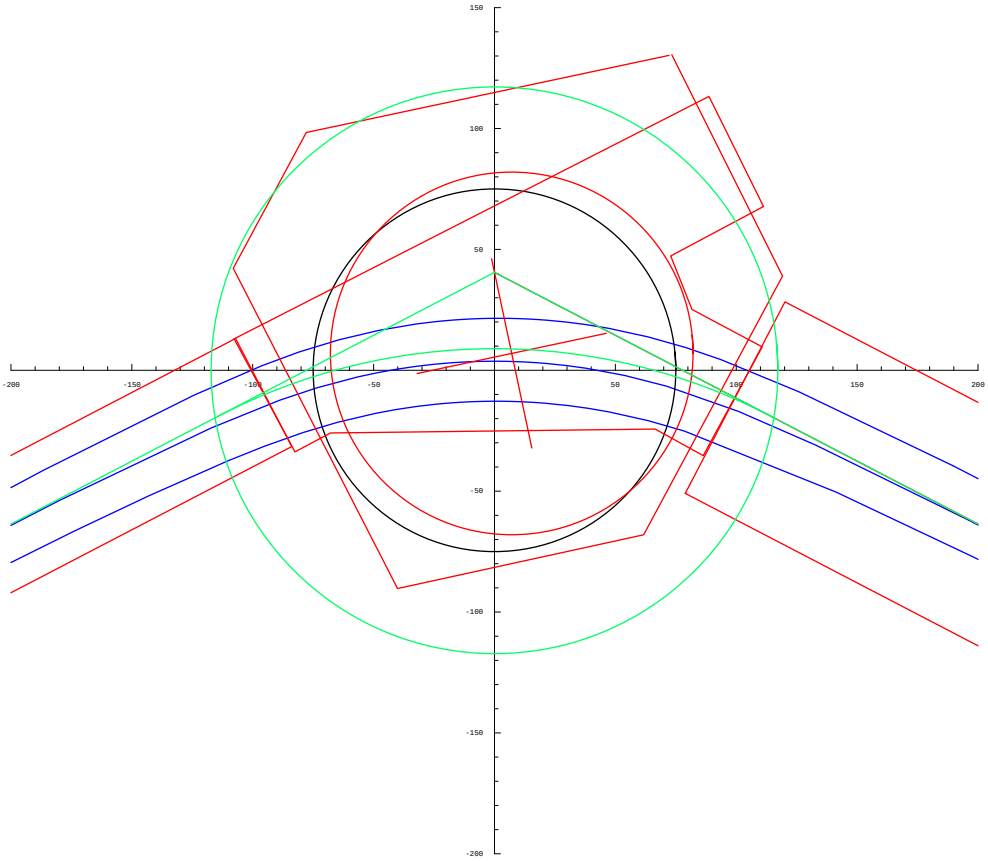

FIG. 14: Trajectories and vacuum chamber, in the vicinity of the round pole spectrometer. The blue lines are the calculated trajectories; the center line is the reference orbit, and the other two lines represent trajectories which differ from the reference orbit by ±15 mrad. The black 75 mm radius circle corresponds to the magnet's pole. The red straight lines are the vacuum chamber. The red circle represents the original location of the magnet's pole, centered at the red cross-hairs. The required position, to which the magnet was moved, is at the origin. The green lines represent the ideal reference orbit, and its extensions; the green circle is the effective radius of the equivalent hard-edge field. Dimensions are in mm.

of the round pole magnet is indicated by the yellow crosshairs; the required position of the center is at the origin. The total required shift of the center of the magnet is about 8 mm in x and 5 mm in y. Fig. 15 shows the complete layout of the round pole spectrometer from object to image

D. Aberrations and momentum resolution

Aberrations to second order have been calculated using the analytical formulae and matrix approach described in [1]. To second order, the dependence of the position at the image on the trajectory initial angles u'_0 and z'_0,

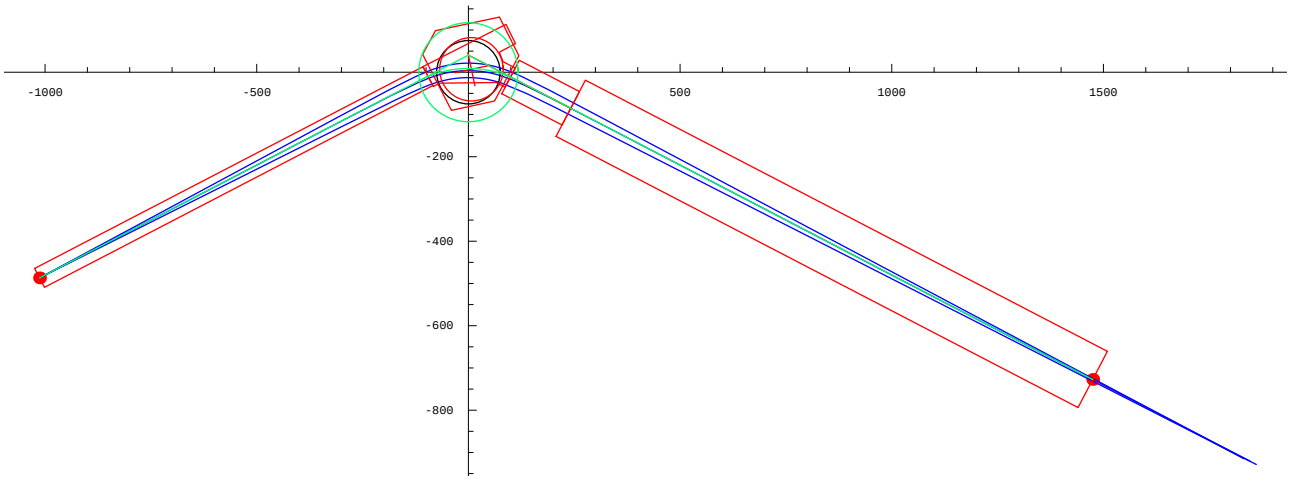

FIG. 15: Round pole spectrometer: trajectories (blue line) and vacuum chamber (red lines), showing object and image (red dots). Dimensions are in mm.

and the momentum deviation $\frac{\delta p}{p}$, are given by

$$u_i = F_{001}\frac{\delta p}{p} + F_{200}\left(u_0'\right)^2 + F_{020}\left(z_0'\right)^2 + F_{101}\frac{\delta p}{p}u_0' + F_{002}\left(\frac{\delta p}{p}\right)^2 \tag{7}$$

$$z_i = G_{010}z_0' + G_{011}\frac{\delta p}{p}z_0' + G_{110}z_0'u_0' \tag{8}$$

in which u_i is the bend-plane transverse coordinate , and z_i is the non-bend-plane transverse coordinate, both evaluated at the bend-plane image point. The nomenclature chosen for the higher order coefficients associates a coefficient (F_{ijk},G_{ijk}) with the dependence of (u_i, z_i) on $\left(u_0'\right)^i\left(z_0'\right)^j\left(\frac{\delta p}{p}\right)^k$.

Aberration effects have also been calculated using the numerical techniques based on the measured field described above in Section III C 1. A series of trajectories, spanning a range of initial angles in u_0' and z_0' of ± 15 mrad, and a range in $\frac{\delta p}{p}$ of $\pm 5\%$, have been numerically computed, and the dependence of u_i and z_i on u_0', z_0' and $\frac{\delta p}{p}$ has been fit to functions of the form

$$\begin{aligned} u_i = {} & F_{100}u_0' + F_{001}\frac{\delta p}{p} + F_{200}\left(u_0'\right)^2 + F_{020}\left(z_0'\right)^2 + F_{101}\frac{\delta p}{p}u_0' + F_{002}\left(\frac{\delta p}{p}\right)^2 \\ & + F_{300}\left(u_0'\right)^3 + F_{120}\ u_0'\ \left(z_0'\right)^2 + F_{201}\frac{\delta p}{p}\left(u_0'\right)^2 + F_{102}\left(\frac{\delta p}{p}\right)^2 u_0' + F_{021}\frac{\delta p}{p}\left(z_0'\right)^2 + F_{003}\left(\frac{\delta p}{p}\right)^3 \\ & + F_{400}\left(u_0'\right)^4 + F_{220}\left(u_0'\right)^2\left(z_0'\right)^2 + F_{040}\left(z_0'\right)^4 + F_{301}\frac{\delta p}{p}\left(u_0'\right)^3 + F_{121}\frac{\delta p}{p}u_0'\ \left(z_0'\right)^2 \\ & + F_{202}\left(\frac{\delta p}{p}\right)^2\left(u_0'\right)^2 + F_{022}\ \left(\frac{\delta p}{p}\right)^2\left(z_0'\right)^2 + F_{103}\left(\frac{\delta p}{p}\right)^3 u_0' + F_{004}\left(\frac{\delta p}{p}\right)^4 \end{aligned}$$

and

$$\begin{aligned} z_i = {} & G_{010}z_0' + G_{110}z_0'u' + G_{011}\frac{\delta p}{p}z_0' + G_{210}\left(u_0'\right)^2 z_0' + G_{030}\left(z_0'\right)^3 + G_{111}\frac{\delta p}{p}z_0'u_0' + G_{012}\left(\frac{\delta p}{p}\right)^2 z_0' \\ & + G_{130}u_0'\left(z_0'\right)^3 + G_{310}\left(u_0'\right)^3 z_0' + G_{211}\frac{\delta p}{p}\left(u_0'\right)^2 z_0' + G_{031}\frac{\delta p}{p}\left(z_0'\right)^3 + G_{112}\left(\frac{\delta p}{p}\right)^2 z_0'u_0' + G_{013}\left(\frac{\delta p}{p}\right)^3 z_0' \end{aligned}$$

These are the most general forms, consistent with midplane symmetry of the field, up to fourth order. Tables III and IV present the second order numerical fit coefficients, together with the analytical results. The second order fit coefficients generally agree well with the second order analytic results.

The higher order coefficients quantify cubic and quartic nonlinearities; these are given in Tables IV- VII.

TABLE III: Round pole spectrometer, linear and second order bend-plane aberration coefficients

Calculation	F_{100} mm	F_{001} mm	F_{200} mm	F_{020} mm	F_{101} mm	F_{002} mm
Analytical	0.0	1578	62065	-70074	10092	-1430
Numerical	-2.2	1540.05	77419	-78866	10672	-1336

TABLE IV: Round pole spectrometer, linear, second and third order non-bend-plane aberration coefficients

Calculation	G_{010} mm	G_{110} mm	G_{011} mm	G_{210} mm	G_{030} mm	G_{111} mm	G_{012} mm
Analytical	0.0	-139281	2545				
Numerical	2.1	-154169	181	358988	-315837	124057	1822

TABLE V: Round pole spectrometer, third order bend-plane aberration coefficients,

F_{300} mm	F_{120} mm	F_{201} mm	F_{102} mm	F_{021} mm	F_{003} mm
527262	295946	-5415	-15070	65328	817

TABLE VI: Round pole spectrometer, fourth order bend-plane aberration coefficients

F_{400} mm	F_{220} mm	F_{040} mm	F_{301} mm	F_{121} mm	F_{202} mm	F_{022} mm	F_{103} mm	F_{004} mm
-139925	-1.127×10^7	1.83×10^6-965377	-1.47×10^6	-152119	27245	21883	-528	

TABLE VII: Round pole spectrometer, fourth order non-bend-plane aberration coefficients

G_{130} mm	G_{310} mm	G_{211} mm	G_{031} mm	G_{112} mm	G_{013} mm
9.97×10^6	5.19×10^6	-822292	805652	-110855	-3783

IV. DESIGN OF THE PACMAN SPECTROMETER

A. Geometry and linear optics

The geometry of the small C-magnet (pacman) is shown in Fig. 16. For a given field (i.e, fixed B_0 and L), and a given bend angle α, there is a unique value of the bend radius corresponding to the trajectory illustrated in Fig. 16. We have for the bend radius

$$\rho = \frac{L}{2\sin\frac{\alpha}{2}} \tag{9}$$

and the central momentum can then be calculated from Eq. (2). The angles in Fig. 16 are related by $\gamma = \alpha - 2\beta$.

The value of the bend radius can then be substituted into the transport matrices. The value of the angle β is the only remaining free parameter. If one were designing a new magnet, this angle would be varied to find a value corresponding to the condition of double focusing at the image point. This value will depend on the object distance S_o. In the case of the existing pacman magnet, the value of β is already determined. Hence we would not necessarily expect to realize the exact double focusing condition. However, as described below, we are not far off.

The coordinates of the object and image are given by

$$x_o = -s_o\cos\frac{\alpha}{2} - \rho\sin\frac{\alpha}{2} = -S_o\cos\frac{\alpha}{2} \tag{10}$$

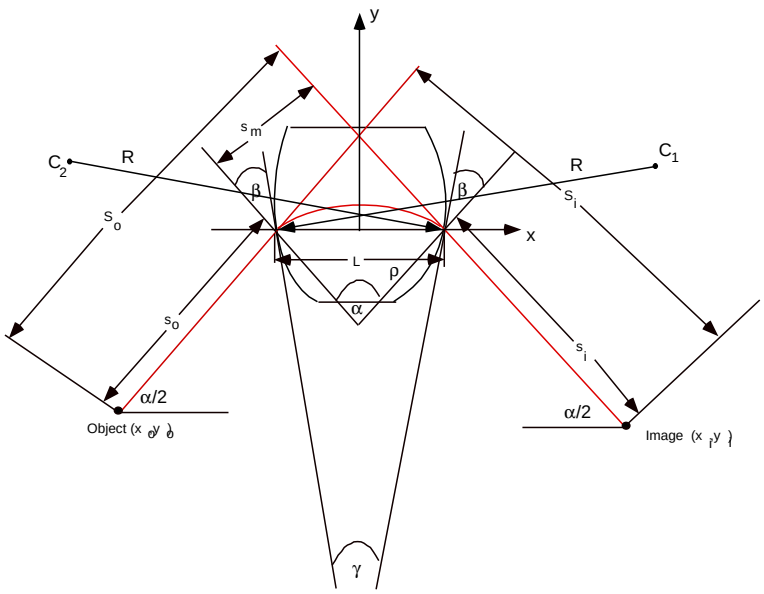

FIG. 16: Geometry of the pacman magnet

$$y_o = -s_o \sin\frac{\alpha}{2} \tag{11}$$

and of the image, by

$$x_i = s_i \cos\frac{\alpha}{2} + \rho \sin\frac{\alpha}{2} = S_i \cos\frac{\alpha}{2}$$
$$y_i = -s_i \sin\frac{\alpha}{2}$$

with $s_m = \rho \tan\frac{\alpha}{2}$, $S_o = s_o + s_m$, $S_i = s_i + s_m$.

For the pacman magnet, the bend angle is $\alpha = 90°$, and an estimate of of the edge angle, based on a direct measurement of the pole tip geometry, is $\beta = 28.25°$. The magnetic field of the pacman magnet has been measured with a Hall probe. The data are shown in Fig. 17. From this data, the effective length L of the magnet can be estimated.

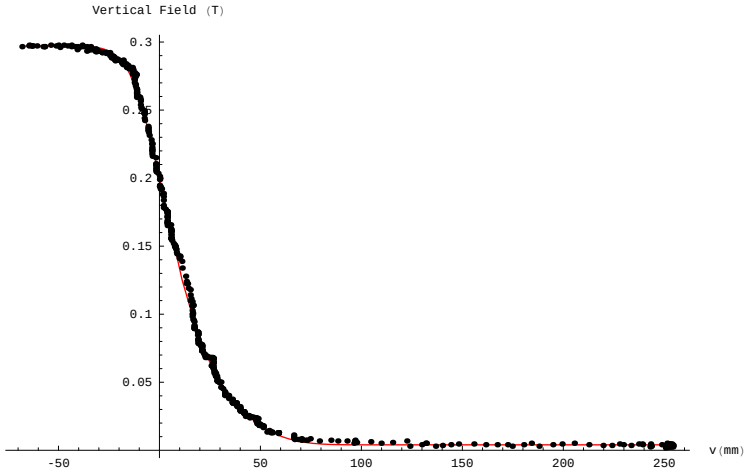

FIG. 17: Measured fringe field of the pacman magnet. The zero of the v coordinate corresponds to the physical edge of the pole tip. Current =150 A. The red line indicates the fitted Enge function, Eq. (12). The best fit parameters were a_1=0.004 T, a_2=0.293 T, a_3=-0.69936, a_4=4.7099, a_5=-2.5752, a_6=1.1388

The effective length is found to be 28.3 mm longer than the physical length across the pole (directly measured to be 258 mm), giving L=286.3 mm. The bend radius can than be found from Eq. (9) to be ρ=202.5 mm.

To evaluate the first order focal properties using Eq. (5) above, we must determine the fringing field integral, Eq. (1), which can be found from Fig. 17. The magnet gap is 44 mm, and the fringing field integral is found to be K=0.328. From Fig. 1, the object distance S_o = 1921 mm. The image distances can then be determined from Eq. (6) above. The image distance in the bend plane is found to be S_{iu}=407.1 mm, and in the non-bend plane it is S_{iz} =397.4 mm. Although the bend plane and non-bend-plane focus occur at different distances, the performance is not significantly degraded due to this, since the aberrations dominate. This is discussed below in Section IV D.

B. Linear lattice functions

Using the same assumptions as stated in Sec. III B, above, we can calculate the evolution of the lattice functions, and the associated beam sizes, through the pacman spectrometer. Fig. 18 shows the lattice functions, and Fig. 19 the beam sizes, given by $\sigma = \sqrt{\varepsilon\beta}$. The dispersion is shown in Fig. 20.

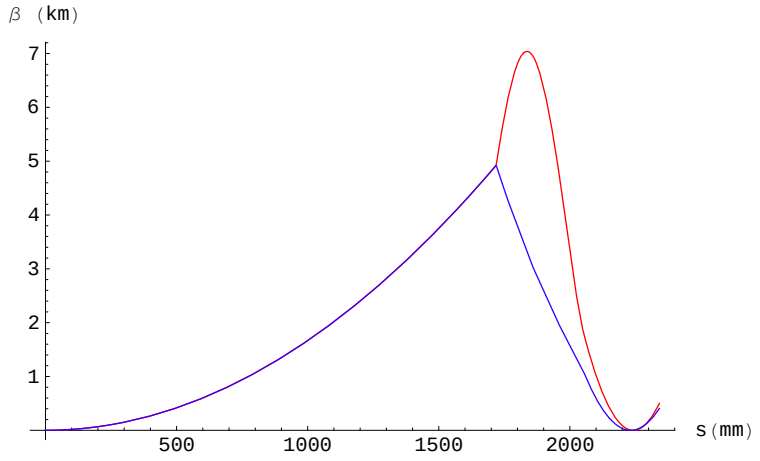

FIG. 18: Lattice functions β_x (red) and β_y (blue) for the pacman spectrometer system

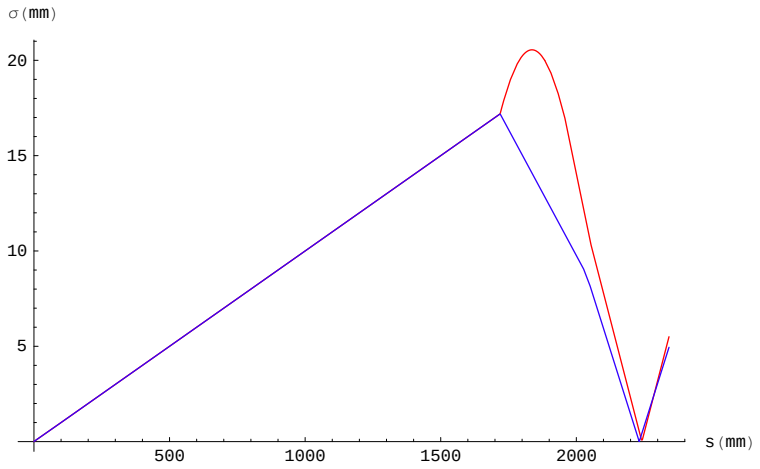

FIG. 19: Rms beam sizes σ_x (red) and σ_y (blue) for the pacman spectrometer system

C. Direct integration of the equations of motion

The technique discussed above in Section III C 1 for the numerical integration of the equations of motion for the round pole magnet may be applied to the pacman magnet, using the measured field given in Fig. 17. In

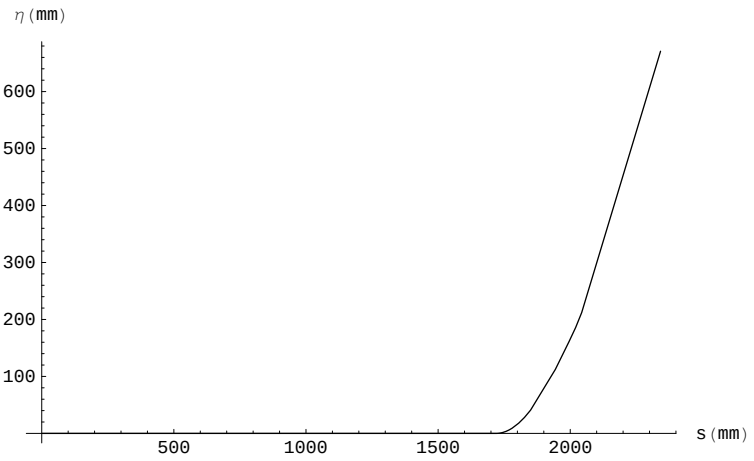

FIG. 20: Dispersion function η for the pacman spectrometer system

this case, the field was fitted to an Enge-type function of the form

$$B_m(v) = a_1 + \frac{a_2}{1 + \exp\left(a_3 + a_4\frac{v}{G} + a_5\left(\frac{v}{G}\right)^2 + a_6\left(\frac{v}{G}\right)^3\right)} \tag{12}$$

with G=magnet gap=44 mm. The resulting fit is shown in Fig. 17. The only additional complication is in the treatment of the pole edges. Each pole edge is considered to be a segment of the arc of a circle of radius R. (See Fig. 16). The left edge has a center at C_1, and the right edge has a center at C_2. The coordinates of the centers are

$$x_{C_1} = R\cos\frac{\gamma}{2} - \frac{L}{2},\ \ x_{C_2} = -x_{C_1},\ \ y_{C_1} = y_{C_2} = y_C = R\sin\frac{\gamma}{2}$$

Let the measured vertical magnetic field shown in Fig. 17 be $B_m(v)$, with v=0 at the pole tip edge. Then the magnetic field at a distance r from the appropriate center point C is

$$B_{z0}(r) = B_m(r - R).$$

Using this field, the vertical and radial field components may be calculated as described above in Section III C 1. The field coordinates in the Cartesian system shown in Fig. 16 are then derived using

$$B_x(x,y,z) = \frac{(x - x_C)\,B_r\left(\sqrt{(x-x_C)^2 + (y-y_C)^2}, z\right)}{\sqrt{(x-x_C)^2 + (y-y_C)^2}}$$

$$B_y(x,y,z) = \frac{(y - y_C)\,B_r\left(\sqrt{(x-x_C)^2 + (y-y_C)^2}, z\right)}{\sqrt{(x-x_C)^2 + (y-y_C)^2}}$$

$$B_z(x,y,z) = B_z\left(\sqrt{(x-x_C)^2 + (y-y_C)^2}, z\right)$$

in which $C = C_2$ if $x < 0$ and $C = C_1$ if $x > 0$. The equations of motion have been solved starting at the point given by Eq. (10) and (11), with $\alpha = 90°$, S_o =1921 mm, and s_o = 1720 mm. The radius of curvature of the pole tip is estimated as follows. On Drawing 18M653, of the proposed new pacman magnet, the pole tip radius is indicated as 1086 mm. Since the existing pacman is purported to be a half-scale version of this, we take the pole tip radius to be about half this: R=530 mm. (A direct measurement from the curvature of the pole tip gives a radius of curvature of 520 mm, with a few tens of mm error). This defines the magnet geometry fully. We take the central field to be B_0=0.297 T (from Fig. 20), corresponding to 150 A in the magnet. Numerical solution of the central trajectory then gives ρ=200.2 mm, implying a central momentum of 17.83 MeV/c for this field. The images are found at the distances (S_{iu}, S_{iz}) =(410.7, 396) mm. The trajectories are shown in Fig. 21. From Fig. 1, the phosphor screen for viewing the beam is located at S=402.5, very close to the average focal point. The geometry and first order optical properties of the pacman spectrometer are summarized in Tables VIII and IX.

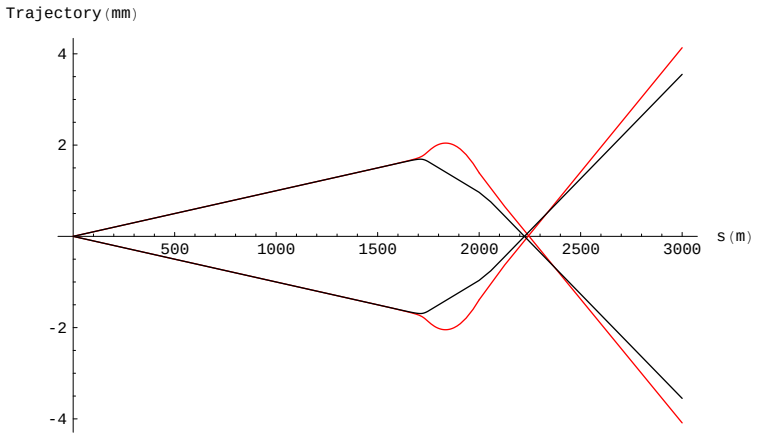

FIG. 21: Trajectories computed by numerical integration, for the measured field of the pacman magnet. The red curves correspond to trajectories in the bend plane, relative to the reference trajectory; the initial values are $u_0' = \pm 1$ mrad. The black curves are trajectories in the non-bend plane, corresponding to $z_0' = \pm 1$ mrad.

TABLE VIII: Pacman spectrometer geometrical parameters

Magnet	α	β	ρ	B_0	p_0	G	K	R	L	Δ
	deg.	deg.	mm	T	MeV/c	mm		mm	mm	mm
Hard edge approx.	90	28.25	202.46	0.297	18.03	44	0.3278	530	286.32	0
Exact numer. int.	90	28.25	200.205	0.297	17.826				283.13	0

TABLE IX: Pacman spectrometer first order optical parameters

Magnet	S_0	f_u	f_z	S_{iu}	S_{iz}	$T_{11}\,(s_{iu}, s_o)^a$	$T_{33}\,(s_{iz}, s_o)^{\ b}$
	mm	mm	mm	mm	mm		
Hard edge approx.	1921	284.6	356.0	407.1	397.4	-0.18	-0.25
Exact numer. int.	1921			410.7	396.0		

[a] Horizontal magnification
[b] Vertical magnification

D. Aberrations

Aberrations to second order have been calculated using the analytical formulae and matrix approach described in [1]. As discussed above in Section III D, a series of trajectories, spanning a range of initial angles in u_0' of ± 15 mrad and in z_0' of ± 9 mrad, and a range in $\frac{\delta p}{p}$ of $\pm 5\%$, have been numerically computed, and the dependence of u_i and z_i on u_0', z_0' and $\frac{\delta p}{p}$ has been fit to functions of the form described in Section III D. Tables X and XI presents the results of the second order numerical fit coefficients, together with the analytical results. The second order fit coefficients agree well with the second order analytic results. The higher order coefficients quantify cubic and quartic nonlinearities; these are given in Tables XI- XIV.

V. PERFORMANCE OF THE ROUND POLE SPECTROMETER

A. Dynamic range

The dynamic range of the spectrometer is the range of momenta which can be measured with a given setting of the magnet current. This is determined by the dispersion at the focus, and by the range of physically observable distance in the bend plane at the focus. The window on which the beam will be observed is about 140 mm

TABLE X: Pacman, linear and second order bend-plane aberration coefficients

Calculation	F_{100} mm	F_{001} mm	F_{200} mm	F_{020} mm	F_{101} mm	F_{002} mm
Analytical	0.0	517	-265	-13334	5049	-459
Numerical	0.22	510.7	-11.8	-11621	4976	-449

TABLE XI: Pacman, linear, second and third order non-bend-plane aberration coefficients

Calculation	G_{010} mm	G_{110} mm	G_{011} mm	G_{210} mm	G_{030} mm	G_{111} mm	G_{012} mm
Analytical	-41	-33885	2482				
Numerical	-66	-29507	2040	38027	-749725	-3151	-1185

TABLE XII: Pacman spectrometer, third order bend-plane aberration coefficients

F_{300} mm	F_{120} mm	F_{201} mm	F_{102} mm	F_{021} mm	F_{003} mm
60985	-90579	17075	-6263	13719	473

TABLE XIII: Pacman spectrometer, fourth order bend-plane aberration coefficients

F_{400} mm	F_{220} mm	F_{040} mm	F_{301} mm	F_{121} mm	F_{202} mm	F_{022} mm	F_{103} mm	F_{004} mm
327329	122138	618002	33370	-90579	-34558	-15272	6877	-508

TABLE XIV: Pacman spectrometer, fourth order non-bend-plane aberration coefficients

G_{130} mm	G_{310} mm	G_{211} mm	G_{031} mm	G_{112} mm	G_{013} mm
932161	1.20×10^{6}	-623496	75922	57889	-174

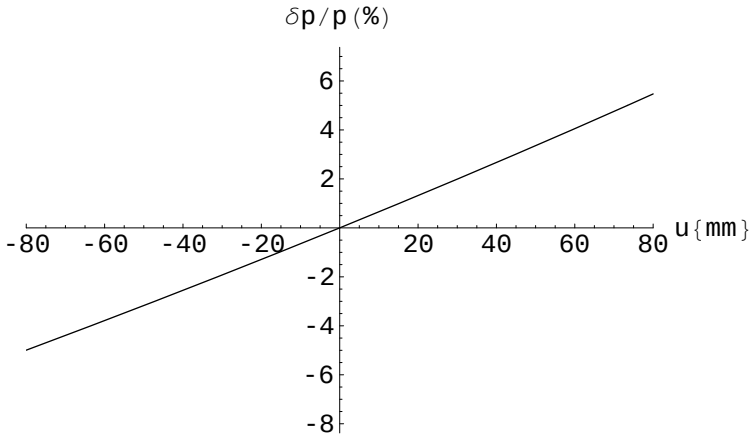

FIG. 22: Relative momentum vs. distance at the focus

wide. Fig. 22 shows the calculated relative momentum vs. distance at the focus. From that figure, the dynamic range of the spectrometer is roughly -4.5% to 5%.

B. Central momentum vs. magnet current

Neglecting saturation effects, there is a linear relation between the central momentum and the magnet current. The central momentum is 49.74 MeV/c for a central field of 0.67 T, which is attained at a current of 35 A. Thus, the relation between the central momentum and the current, neglecting saturation, is

$$p\left[\frac{\mathrm{MeV}}{\mathrm{c}}\right] = 1.421 I\,[\mathrm{A}]\,.$$

The published curves[5] of field vs. current, for a 58 mm gap, indicate that the magnet is not saturated at 35 A, so this linear relation should be accurate for lower currents.

C. Momentum resolution

To second order, the dependence of the horizontal trajectory co-ordinate at the focus on the momentum deviation and the initial trajectory angles at the source is given by Eq. (7):

$$u_i = F_{001}\frac{\delta p}{p} + F_{200}\left(u_0'\right)^2 + F_{020}\left(z_0'\right)^2 + F_{101}\frac{\delta p}{p}u_0' + F_{002}\left(\frac{\delta p}{p}\right)^2$$

The last two terms are typically small (see Table III); neglecting these, we can solve for the momentum deviation

$$\frac{\delta p}{p} = \frac{u_i - \left(F_{200}\left(u_0'\right)^2 + F_{020}\left(z_0'\right)^2\right)}{F_{001}}$$

Consider a collection of trajectories, all with the same momentum deviation, and arriving at the same horizontal trajectory coordinate, but starting with different initial angles. The average value of the momentum deviation we would measure is

$$\left\langle\frac{\delta p}{p}\right\rangle = \frac{u_i - \left(F_{200}\left\langle {u_0'}^2\right\rangle + F_{020}\left\langle {z_0'}^2\right\rangle\right)}{F_{001}}$$

The last two terms in the numerator represent a correction to the momentum/position correlation indicated in Fig. 22, due to aberrations. The standard deviation in the momentum measurement is

$$D\left(\frac{\delta p}{p}\right) = \sqrt{\left\langle\left(\frac{\delta p}{p}\right)^2\right\rangle - \left\langle\frac{\delta p}{p}\right\rangle^2} = \frac{1}{F_{001}}\sqrt{F_{200}^2\left(\left\langle {u_0'}^4\right\rangle - \left\langle {u_0'}^2\right\rangle\right) + F_{020}^2\left(\left\langle {z_0'}^4\right\rangle - \left\langle {z_0'}^2\right\rangle\right)}$$

The smallest momentum separation which we can clearly resolve is the momentum resolution. Let us take this to be equal to two standard deviations of the measurement. For a Gaussian distribution in the initial angles, for which $\left\langle {z_0'}^4\right\rangle = 3\left\langle {z_0'}^2\right\rangle^2$, and taking $\left\langle {u_0'}^2\right\rangle \approx \left\langle {z_0'}^2\right\rangle$, the resolution is

$$R = 2D\left(\frac{\delta p}{p}\right) = 2\sqrt{2}\left\langle {z_0'}^2\right\rangle\frac{\sqrt{F_{200}^2 + F_{020}^2}}{F_{001}}.$$

Fig. 23 shows the resolution vs. $\sqrt{\left\langle {z_0'}^2\right\rangle}$ for the round pole spectrometer. The values of the coefficients used have been taken from Table III (exact).

D. Sensitivity of the non-bend-plane aberrations to moments of the source vertical angular distribution

To second order, the non-bend-plane coordinate at the image point is related to the initial angles and the momentum deviation by Eq. (8):

$$z_i = G_{010}z_0' + G_{011}\frac{\delta p}{p}z_0' + G_{110}z_0'u_0'$$

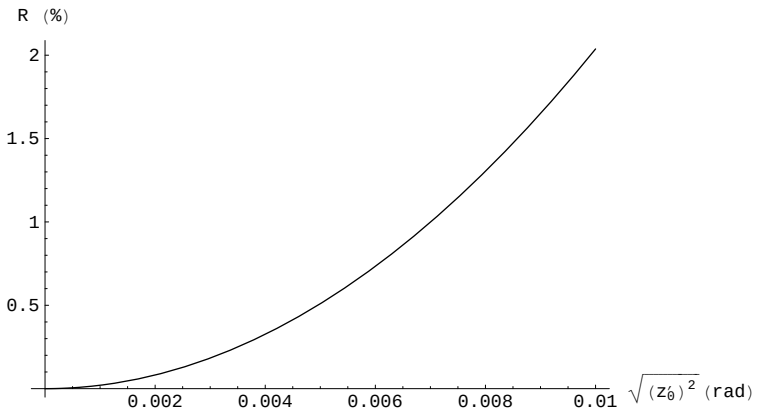

FIG. 23: Momentum resolution (in %) vs. $\sqrt{\left\langle z_0'^{\,2}\right\rangle}$, for the round pole spectrometer

Let us consider the collection of trajectories comprising the beam, and work at the central momentum ($\frac{\delta p}{p} = 0$). The first moment of the distribution at the image point is given by

$$\langle z_i \rangle = G_{010} \langle z_0' \rangle + G_{110} \langle z_0' u_0' \rangle .$$

We would expect that all odd moments of the initial vertical angle distribution would be zero, if the direction of the laser which generates the beam lies in the magnetic median plane. Then

$$\langle z_i \rangle \cong G_{110} \langle z_0' u_0' \rangle$$

If the angular distribution of the electrons emerging from the source is cylindrically symmetric, then there is no correlation between u_0' and z_0', and

$$\langle z_i \rangle \cong G_{110} \langle z_0' \rangle \langle u_0' \rangle = 0$$

If, however, there is an angular asymmetry in the source distribution, so that the horizontal angle is related to the vertical angle by

$$u_0' = \tilde{u}_0' + \varepsilon z_0'$$

in which $\tilde{u}_0'$ is the uncorrelated piece, then

$$\langle z_i \rangle \cong G_{110} \langle z_0' u_0' \rangle = G_{110} \langle z_0' \left(\tilde{u}_0' + \varepsilon z'\right) \rangle = G_{110} \varepsilon \left\langle z_0'^{\,2} \right\rangle \tag{13}$$

The horizontal-vertical coupling represented by the G_{110} aberration coefficient thus manifests itself as a net shift of the vertical position.

The second moment of the distribution at the image point is

$$\begin{aligned} \left\langle z_i^2 \right\rangle &= G_{010}^2 \left\langle z_0'^{\,2} \right\rangle + G_{110}^2 \left\langle z_0'^{\,2} u_0'^{\,2} \right\rangle + 2 G_{010} \left\langle z_0'^{\,2} u_0' \right\rangle \\ &= G_{010}^2 \left\langle z_0'^{\,2} \right\rangle + G_{110}^2 \left\langle z_0'^{\,2} \left(\tilde{u}_0' + \varepsilon z_0'\right)^2 \right\rangle \\ &= G_{010}^2 \left\langle z_0'^{\,2} \right\rangle + G_{110}^2 \left(\left\langle z_0'^{\,2} \right\rangle \langle (\tilde{u}_0')^2 \rangle + \varepsilon^2 \left\langle z_0'^{\,4} \right\rangle \right) . \end{aligned}$$

If we further approximate $\langle (\tilde{u}_0')^2 \rangle \approx \left\langle z_0'^{\,2} \right\rangle$ and $\left\langle z_0'^{\,4} \right\rangle = 3 \left\langle z_0'^{\,2} \right\rangle^2$ (for a Gaussian distribution), then

$$\left\langle z_i^2 \right\rangle \approx G_{010}^2 \left\langle z_0'^{\,2} \right\rangle + G_{110}^2 \left\langle z_0'^{\,2} \right\rangle^2 \left(1 + 3\varepsilon^2\right) . \tag{14}$$

Together with Eq. (13), Eq. (14)may be used to find $\left\langle z_0'^{\,2} \right\rangle$ and ϵ.

To illustrate the sensitivity for the round pole spectrometer, Fig. 24 shows the dependence of $\langle z_i \rangle$ on ϵ, for several values of $\sqrt{\left\langle z_0'^{\,2} \right\rangle}$. Fig. 25 shows the dependence of $\sqrt{\langle z_i^2 \rangle}$ on $\sqrt{\left\langle z_0'^{\,2} \right\rangle}$, for several values of ϵ. In practice, for accurate results the higher order aberration terms must be include in Eq. (13) and Eq. (14). In the figures, the calculations have been done including all terms up to fourth order.

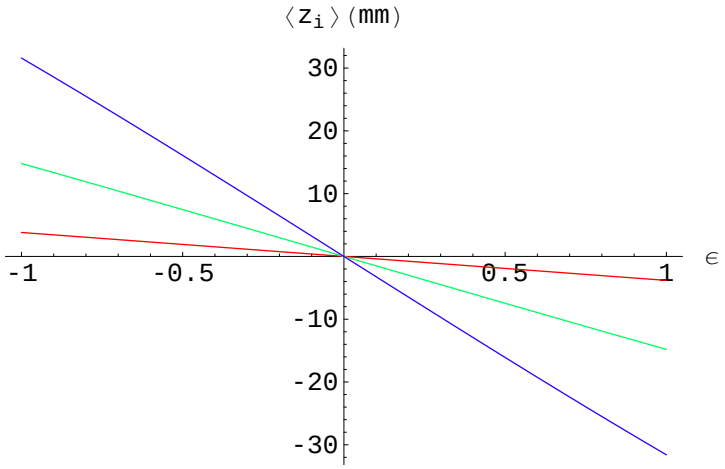

FIG. 24: Dependence of $\langle z_i \rangle$ on ϵ, for several values of $\sqrt{\langle z_0'^2 \rangle}$, for the round pole spectrometer. Red line: $\sqrt{\langle z_0'^2 \rangle}$=3 mrad; green line, $\sqrt{\langle z_0'^2 \rangle}$=6 mrad; blue line $\sqrt{\langle z_0'^2 \rangle}$=9 mrad

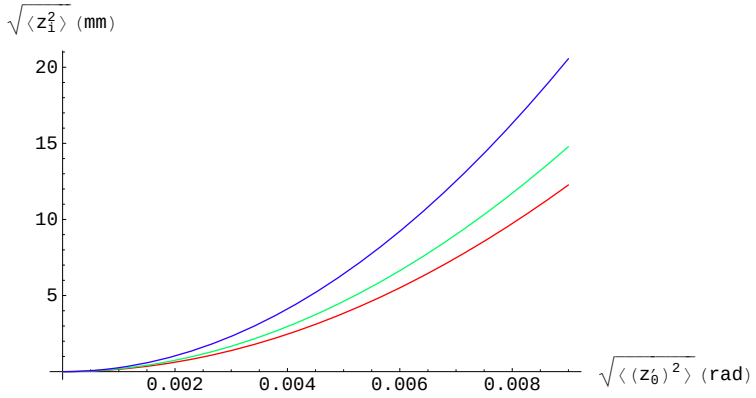

FIG. 25: Dependence of $\sqrt{\langle z_i^2 \rangle}$ on $\sqrt{\langle z_0'^2 \rangle}$, for several values of ϵ, for the round pole spectrometer. Red line: ϵ=0; green line, ϵ=0.5; blue line, ϵ=1

E. Focal point spot size simulations

To provide some estimates of the expected characteristics of the beam spot at the focus, a collection of trajectories representing the beam has been tracked through the spectrometer by numerical solution of the equations of motion. The physical acceptance of the spectrometer, limited by the vacuum chamber, is about ±30 mrad in z' and (+22, -15) mrad in u'. However, as discussed above in Sections V C and V D, allowing such a large range of vertical angles seriously degrades the momentum resolution of the spectrometer, and would result in a vertical spot size of many centimeters. For this reason, we assume that both the initial vertical and horizontal angles are collimated to ±15 mrad. A series of 300 trajectories has been calculated, corresponding to a point source, with a uniform distribution in u_0' and in z_0' over the ranges cited above. All these trajectories have a momentum equal to the central momentum. Fig. 26 shows the distribution of these trajectories at the focal point in u and z. Fig. 27 and Fig. 28 show the histograms of the projections of this distribution onto the u and z axes.

These calculations were repeated for 300 trajectories with momenta 2% higher, and 2% lower, than the reference momentum. Fig. 29 shows the distribution of these trajectories at the focal point in u and z. Fig. 30 shows the histogram of the projection of this distribution onto the u axis.

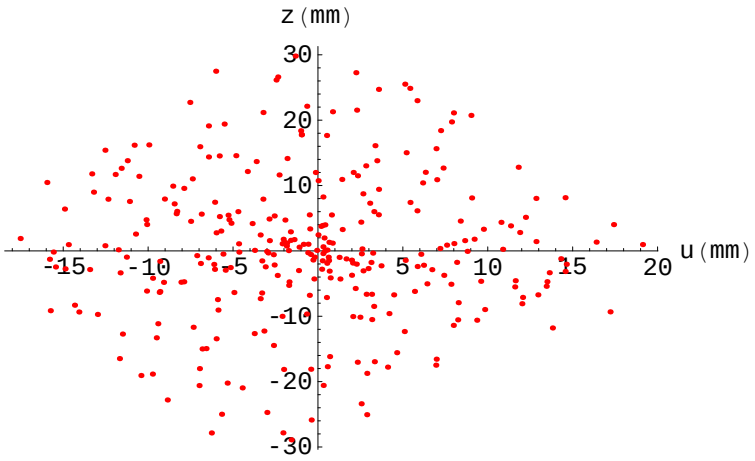

FIG. 26: Distribution of 300 trajectories at the focus, in u and z

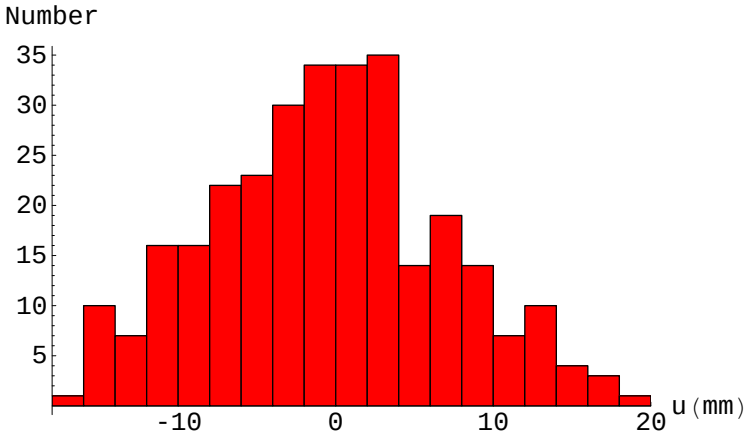

FIG. 27: Histogram of the projection of Fig. 26 onto the u-axis. The standard deviation is 7.4 mm.

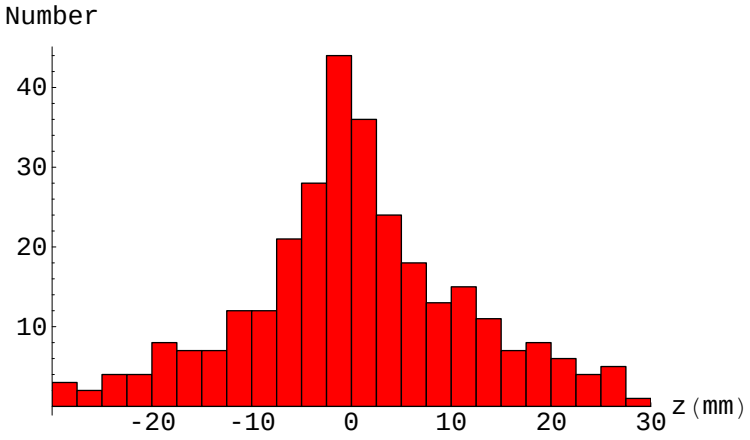

FIG. 28: Histogram of the projection of Fig. 26 onto the z-axis. The standard deviation is 11.2 mm.

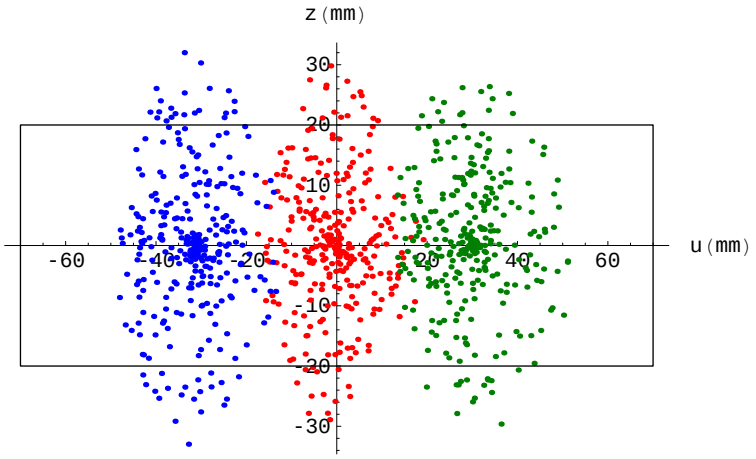

FIG. 29: Distribution of trajectories at the focus, in u and z, for three different momenta (red: central momentum; green: 2% high; blue, 2% low). The rectangle indicates the outline of the phosphor screen on which the beam will be observed.

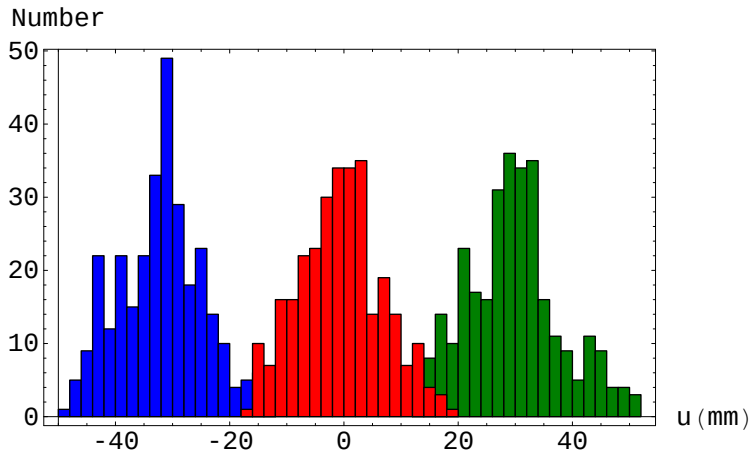

FIG. 30: Histogram of the projection of Fig. 29 onto the u-axis

VI. PERFORMANCE OF THE PACMAN SPECTROMETER

A. Dynamic range and central momentum vs. magnet current

1. *Dynamic range*

The dynamic range of the spectrometer, the range of momenta which can be measured with a given setting of the magnet current, is determined by the dispersion at the focus, and by the range of physically observable distance in the bend plane at the focus. The window on which the beam will be observed is about 65 mm wide. Fig. 31 shows the calculated relative momentum vs. distance at the focus. From that figure, the dynamic range of the spectrometer is roughly -7% to $+7\%$.

2. *Central momentum vs. magnet current*

Using ρ=200.2 mm and Eq. (2), the relation between the momentum and the central field is given by

$$p\left[\frac{\mathrm{MeV}}{\mathrm{c}}\right] = 60.02B\,[\mathrm{T}]$$

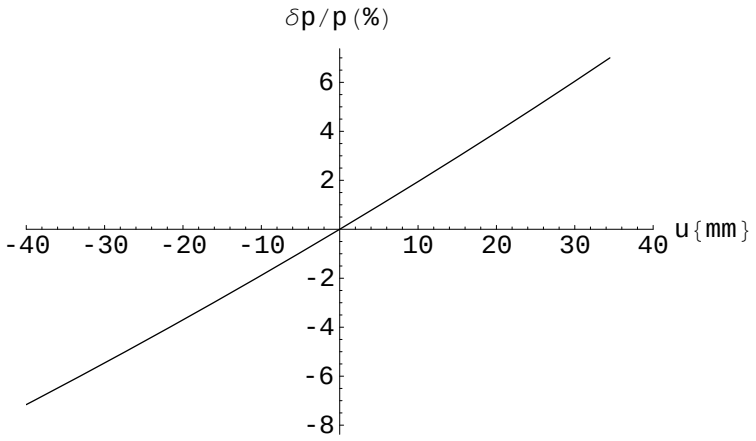

FIG. 31: Relative momentum vs. distance at the focus for the pacman spectrometer

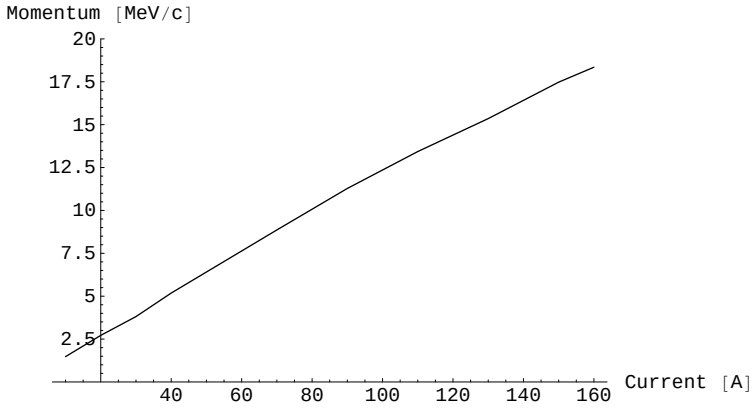

FIG. 32: Relation between current and central momentum, for the pacman magnet

The central field of the magnet has been measured vs. current with a Hall probe. Using this information, and the relation above, Fig. 32 shows the relationship between the central momentum and the magnet current.

The DC resistance of the magnet was measured to be 75 mΩ. When cooled with a water flow of 0.27 $\frac{\text{gal}}{\text{min}}$, the temperature rise across the magnet was measured to be $\Delta T[^\circ\text{C}] = 0.00124\,(I[\text{A}])^2$. Operation beyond about 160 A results in temperature rises above 30° C and is not recommended.

B. Momentum resolution

We use the same definition of momentum resolution as described in Sec. V C above. Fig. 33 shows the momentum resolution vs. $\sqrt{\left\langle {z_0'}^2 \right\rangle}$ for the pacman spectrometer. The values of the coefficients used have been taken from Table X (exact).

C. Sensitivity of the non-bend-plane aberrations to moments of the source vertical angular distribution

To illustrate these sensitivities for the pacman spectrometer, Fig. 34 shows the dependence of $\langle z_i \rangle$ on ϵ, for several values of $\sqrt{\left\langle {z_0'}^2 \right\rangle}$. Fig. 35 shows the dependence of $\sqrt{\langle z_i^2 \rangle}$ on $\sqrt{\left\langle {z_0'}^2 \right\rangle}$, for several values of ϵ. In all

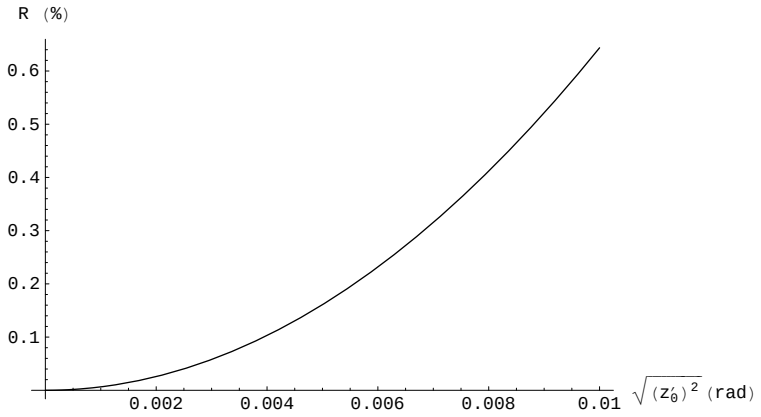

FIG. 33: Momentum resolution (in %) vs. $\sqrt{\langle z_0'^2 \rangle}$, for the pacman spectrometer

cases, the calculations have been done including all terms up to fourth order.

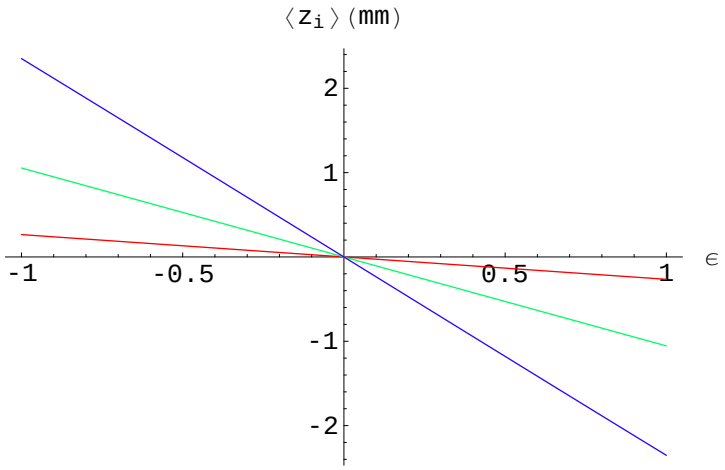

FIG. 34: Dependence of $\langle z_i \rangle$ on ϵ, for several values of $\sqrt{\langle z_0'^2 \rangle}$, for the pacman spectrometer. Red line: $\sqrt{\langle z_0'^2 \rangle}$=3 mrad; green line, $\sqrt{\langle z_0'^2 \rangle}$=6 mrad; blue line $\sqrt{\langle z_0'^2 \rangle}$=9 mrad

D. Focal point spot size simulations

A collection of trajectories has also been tracked through the pacman spectrometer. The acceptance of the magnet is limited by the size of the vacuum chamber at the magnet entrance, which imposes the limits $|u'| < 15$ mrad, and $|z'| < 9$ mrad. A series of 300 trajectories has been calculated, corresponding to a point source, with a uniform (random) distribution in u and in z over the ranges cited above. All these trajectories have a momentum equal to the central momentum. Fig. 36 shows the distribution of these trajectories at the (horizontal) focal point in u and z. Fig. 37 and Fig. 38 show the histograms of the projections of this distribution onto the u and z axes.

These calculations were repeated for 300 trajectories with momenta 1% higher, and 1% lower, than the reference momentum. Fig. 36 shows the distribution of these trajectories at the focal point in u and z. Fig. 40 shows the histogram of the projection of this distribution onto the u axis.

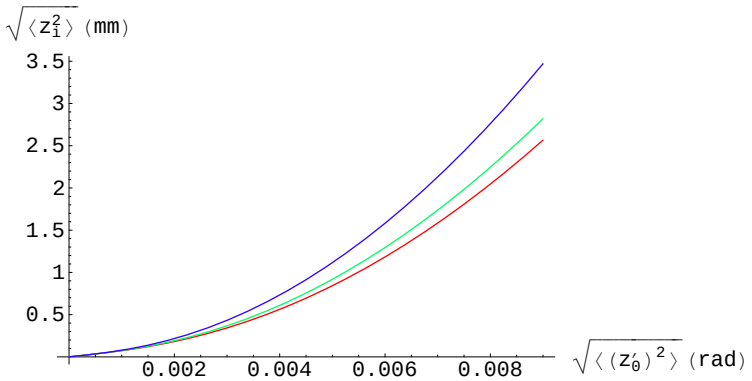

FIG. 35: Dependence of $\sqrt{\langle z_i^2 \rangle}$ on $\sqrt{\langle z_0'^2 \rangle}$, for several values of ϵ, for the pacman spectrometer.Red line: ϵ=0; green line, ϵ=0.5; blue line, ϵ=1

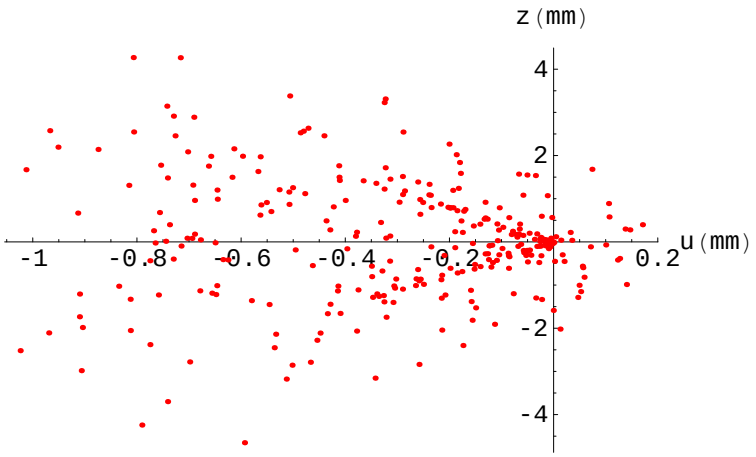

FIG. 36: Distribution of trajectories at the focus, in u and z

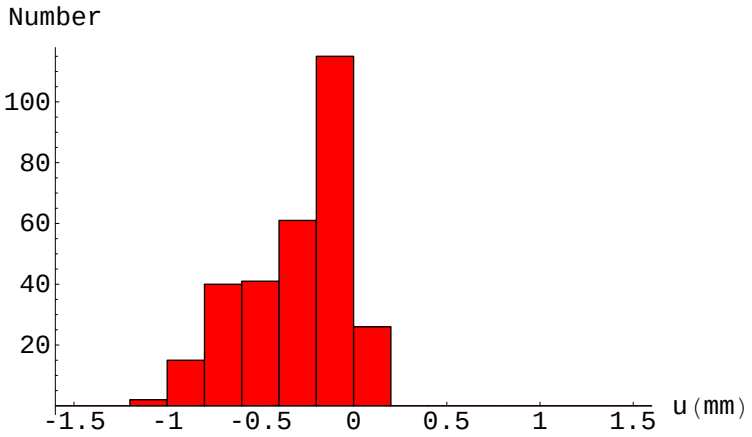

FIG. 37: Histogram of the projection of Fig. 36 onto the u-axis. The standard deviation is 0.3 mm.

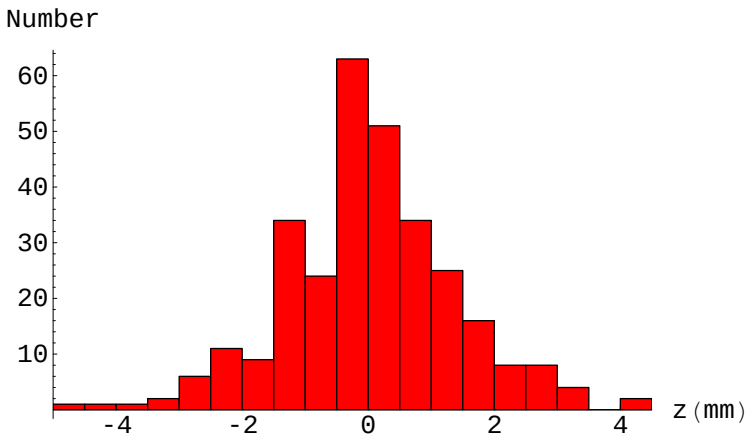

FIG. 38: Histogram of the projection of Fig. 36 onto the z-axis. The standard deviation is 1.4 mm

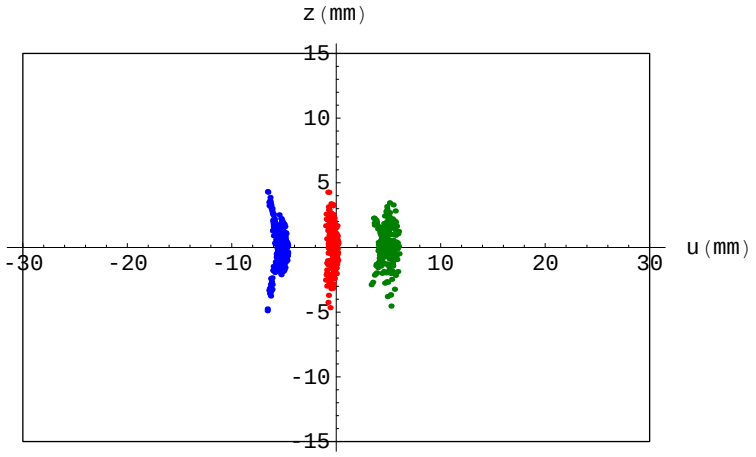

FIG. 39: Distribution of trajectories at the focus, in x and y, for three different momenta (red: central momentum; green: 1% high; blue, 1% low). The rectangle indicates the outline of the phosphor screen on which the beam will be observed.

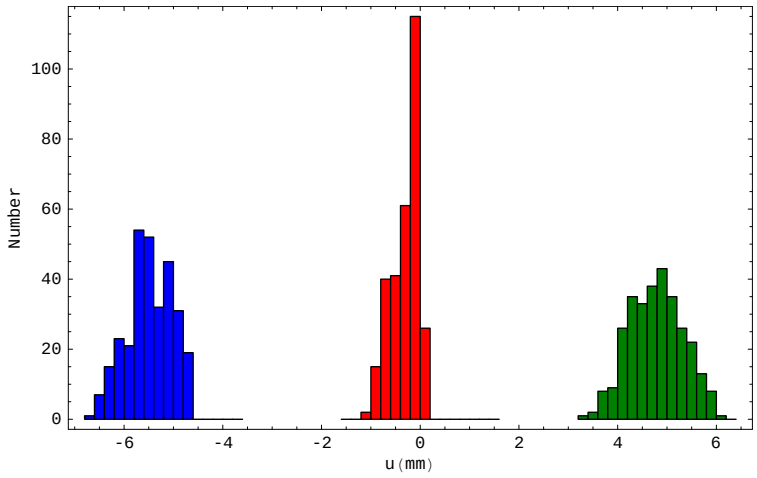

FIG. 40: Histogram of the projection of Fig. 39 onto the u-axis

VII. CONCLUSION

Two magnetic spectrometers will be used to momentum analyze the electron beam produced by the l'OASIS laser wakefield accelerator. In this note, the optical design of the spectrometers is described, and performance features of these spectrometers have been analyzed. One spectrometer, which uses a magnet with a round pole, is capable of momentum analysis with a maximum central momentum in excess of 50 MeV/c. For a given setting of the field, it has a dynamic range of about 11%, acceptance (limited by aberrations) of about ±15 mrad, and momentum resolution of about 1.5% at this acceptance. The other spectrometer is limited in momentum analysis capabilities to a maximum central momentum of about 18 MeV/c. For a given setting of the field, it has a dynamic range of about 14% and an acceptance (limited by vacuum chamber) of about ±15 mrad in the bend plane and ±9 mrad in the non-bend plane. It has a momentum resolution of about 0.5% at this acceptance.

Acknowledgments

The authors would like to thank Matthaeus Leitner of LBNL for useful discussions on the design of magnetic spectrometers.

---

[1] K. L. Brown, "A first and second order matrix theory for the design of beam transport systems and charged particle spectrometers," Tech. Rep. SLAC-75, Rev. 4, SLAC, 1975.
[2] F. C. Iselin, "Lie transformations and transport equations for combined function dipoles," *Part. Accel.*, vol. 17, pp. 143–155, 1985.
[3] A. Misuri, L. Hand, W. Leemans, and G. Fubiani, "Design of a double focusing spectrometer for advanced acceleration experiments."
[4] A. Misuri, M. Leitner, and W. Leemans, "Report on the round poles."
[5] *Users Manual, GMW Associates Laboratory Electromagnet Model 3473-70.*